UNIVERSITY OF CALIFORNIA
RIVERSIDE

Advanced Structural and Electrochemical Methods Toward Next Generation High Capacity Lithium Ion Batteries

A Dissertation submitted in partial satisfaction
of the requirements for the degree of

Doctor of Philosophy

in

Mechanical Engineering

by

Rachel Ye

June 2018

Dissertation Committee:
Dr. Cengiz S. Ozkan, Co-Chairperson
Dr. Mihri Ozkan, Co-Chairperson
Dr. Marko Princevac
Dr. Kambiz Vafai

The Dissertation of Rachel Ye is approved:

_____

_____

_____

Committee Co-Chairperson

_____

Committee Co-Chairperson

University of California, Riverside

Copyright Acknowledgements

The text and figures in Chapter 2, in part or in full, are a reprint of the material as it appears in the published work: Bell, Jeffrey, **Ye, Rachel** et al., “Free-standing Ni-NiO Nanofiber Cloth Anode for High Capacity, High Rate Li-ion Batteries” ***Nano Energy*** 18 (2015): 47-56.

The text and figures in Chapter 3, in part or in full, are a reprint of the material as it appears in the published work: **Ye, Rachel**, et al. "Advanced Sulfur-Silicon Full Cell Architecture for Lithium Ion Batteries." ***Scientific reports*** 7.1 (2017): 17264.

The text and figures in Chapter 4, in part or in full, are a reprint of the material as it appears in the published work: **Ye, Rachel**, et al. "Plateau Targeted Conditioning: An Additive-Free Approach towards Robust SEI Formation in Li-S Batteries for Enhanced Capacity and Cycle Life." ***Nano Energy*** (2018).

Dedicated to my family

ABSTRACT OF THE DISSERTATION

Advanced Structural and Electrochemical Methods Toward Next Generation High Capacity Lithium Ion Batteries

by

Rachel Ye

Doctor of Philosophy, Graduate Program in Mechanical Engineering
University of California, Riverside, June 2018
Dr. Cengiz S Ozkan, Co-Chairperson
Dr. Mihri Ozkan, Co-Chairperson

As the demand for higher capacity, longer lasting lithium ion battery rises, finding a new material system that can replace the current commercial lithium ion battery system has become the necessity. Out of all possible candidates, nickel oxide, silicon shows potential for next generation anode material, and sulfur promises great improvement if used as the cathode material. In this work, new lithium ion battery systems utilizing nickel oxide, silicon, and sulfur were developed and studied using both physical and electrochemical characterization techniques. The free-standing nickel oxide nanofiber cloth anode shows a high capacity of 1054 mAh/g cycling at 20 minuets per charge. It also shows a cycle life of over 1500 cycles. The novel silicon sulfur full cell architecture presents a functioning silicon sulfur system that does not require prelithiation and shows a energy density of 350 Wh/kg for 250 cycles. The novel plateau targeted conditioning method for sulfur half cells shows a 10% increase in battery capacity and great increase in battery stability, as well as proof of stable sei formation on both the anode and cathode.

Table of Contents

List of Figures

List of Tables

Chapter 1: Introduction

Lithium-ion batteries had become the choice for portable electronics and electric vehicles. However, with the development of said electronics, compatible batteries with better performance are in great demand. This demand of higher capacity and longer lasting lithium ion batteries has turned researchers toward new material systems for lithium ion batteries. This is because the existing battery material systems, consisting of graphite as the anode material and metal oxide as the cathode material, are reaching its optimal state, and lacks the potential for a higher capacity battery.[1-7] For example, the best commercial cathode currently in use is NMC, with a theoretical capacity of 276 mAh/g, and the best commercial anode graphite has a theoretical capacity of 372 mAh/g. Although the theoretical energy density for a battery utilizing NMC and graphite is around 633 Wh/kg, this number is purely accounting the weight of the active materials. Current commercial lithium ion batteries' active material weight is approximately 15% to 30% of the total battery weight. This means that, the performance of the current lithium ion batteries utilizing the existing commercial electrodes, about 200 Wh/kg, are already close to its limits, which is 30% of 633Wh/kg. This means a new material system is needed to further improve battery capacity.

1.1 New anode materials for lithium ion batteries

On the anode side of the battery, there are in general two types of anode materials for lithium ion batteries, the alloying materials and the transitional metal oxide materials.

The alloying materials, which are able to alloy with lithium electrochemically and form compound with it, usually have higher theoretical capacities, and a low lithiation potential, but they also have large volume expansions.[8] This means that alloying materials when used in a battery can produce a very high capacity and energy density but lacks the stability a commercial battery requires. The transition metal oxide materials, which forms lithium oxide and metal ions when exposed to lithium ions, usually have relatively lower capacities, high lithiation potentials, but has a much smaller volume expansion. This means that transition metal oxide materials when used in a battery can be very stable and will have a very long cycle life but will have a limited energy density. Some researchers also argue that lithium metal itself can serve as an anode for lithium ion batteries, but it suffers from safety concerns resulting from dendritic formation, electrolyte degradation, and the maximum volumetric change.

There are several kinds of alloying materials that can be utilized as the anode in a lithium ion battery. However, the most concerning ones by researchers and future commercialization markets are tin and silicon. Tin has a theoretical capacity of 960 mAh/g, which is three times the theoretical capacity of graphite, and has enough electric conductivity to withstand battery cycling. However, tin suffers from easy fracturing during volumetric expansion which can result in a fast mechanical degradation, leading to a fast capacity degradation. Silicon on the other hand is the anode material with the highest theoretical capacity, excluding lithium metal itself.[8] However, silicon batteries also need to be improved before they are available for commercialization. The biggest problem of silicon is the volumetric expansion. [9-12] The volume of the silicon can change

400% from its original volume. This can pulverize the electrode and affect the battery's cycle life.[10,11] Other than the volume change, silicon also doesn't have as high of an electrical conductivity as carbon, thus impacting the battery's rate capability.[13] Researchers have utilized methods such as nano structures, conductive networks, and conductive binders to alleviate these issues, but further work needs to be done.[14-20]

Transition metal oxide anode materials can be good candidates for next generation lithium ion batteries as well. One of the most popular transition metal oxide anode is titanium oxide. With a theoretical capacity of 175 mAh/g and a lithiation potential of 1.55V.[8] It has a low energy density capability compared to other anode materials. However, its stability encourages much researchers to use titanium oxide as a additive for other materials. Another metal oxide anode material is nickel oxide. Nickel oxide has a theoretical capacity of 718 mAh/g, which is twice the amount of graphite but has a high lithiation potential of 1.25V.[21] Nickel oxide also shows great stability when used in a battery and is environmentally friendly. Thus, it is a good anode candidate when pairing with a high voltage cathode. In this work, the capability of a nickel oxide fiber electrode was explored and analyzed.

There has been debate over calling pure lithium metal as an anode for lithium ion battery. This is because although lithium metal possesses the highest possible theoretical capacity for lithium ion battery anodes (3860mAh/g), it is also very unstable and can cause a lot of safety concerns.[22] It should not be categorized with any of the two categories mentioned above, because instead of acting as a host for lithium ions, the lithium metal itself is the source of lithium ions. As a result, when all lithium ions travel

to and react with the cathode of the battery, there will be no volume of lithium metal left on the anode side, creating a volumetric change between 0% and 100% of its original volume while other anode materials can only expand and can never has a lower volume than 100%. This can cause a ununiform lithium plating as charge/discharge cycles progress. Another safety issue of lithium metal electrodes is the growth of lithium dendrites. These dendrites forms during charge due to the unstable nature of lithium metal SEI and not only expose more surface area to the electrolyte but also raises the possibility of shorting the battery. These dendrites may also break off and create dead lithium, causing further electrolyte degradation.[23] Which results in a decrease in coulombic efficiency, lifespan, and capacity.

1.2 New cathode materials for lithium ion batteries

In general, all cathode materials for lithium ion batteries can be categorized into two groups, one being the intercalation type cathode, including the commercially available lithium cobalt oxide, and NMC, the other group is the conversion type cathode, which undergoes redox reaction when cycled in a battery.[8] The current state of the art commercial cathode is already reaching the limit of the intercalation type cathodes. This is because for these cathodes, lithium is stored inside its lattice structure as guest ions, which causes minimal volumetric expansion change but also has a limited storage space. These intercalation type cathodes also generally have a high operation voltage, ranging from 4 to 5 V. For the conversion type cathodes however, they are able to react with lithium and can hold much more lithium ions, sulfur, iodine, selenium, and tellurium are

all good examples of the conversion type cathodes. These cathodes generally have a lower operation voltage, ranging from 2 to 3 V, and have much higher theoretical capacities. However, they generally suffer from expansion problems and conductivity problems.

Sulfur, the highest theoretical capacity cathode material and the most promising of the conversion type cathode, suffers from low electrical conductivity, large volumetric expansion, and polysulfide shuttling. [1,2,24-27]Low conductivity is a result of sulfur's insulating properties, this impacts the battery's rate capability when used in a battery. Large volumetric expansion up to 80% of the original volume occurs during discharge, since for each of the sulfur atoms, two lithium atoms are inserted into the original sulfur structure when the battery is completely discharged. [28]This change in volume can cause mechanical degradation of the electrode, which affects the conductive network and solid electrolyte interphase of the electrode.[29] Lastly, polysulfide shuttling results from long chain polysulfides being soluble in the electrolyte.[30] This can cause sulfur to travel across the separator and accumulate on the anode side of the battery. Due to the high theoretical capacity of sulfur, researchers have discovered various methods including mechanical barriers, conductive networks, and chemical suppression, which yields sulfur half cells with promising performance. [29-33]

1.3 New full cell systems for lithium ion batteries

When studying a specific material for lithium ion battery, half-cell formats are usually used to eliminate possible variables that can be caused by the other electrode.

Half-cell format batteries consist of an electrode made out of the material of interest, and a pure lithium counter electrode. Most of the researches on sulfur and silicon are also focused on the half-cell format, this not only because half-cell formats are easier to make, but also because the excess amount of lithium source can prolong the battery life and improve the battery performance. Other than a half cell format, a full cell format which is a complete battery, consists of a cathode and an anode with lithium integrated into the cathode or anode side. Conventional lithium-ion full cells rely on the cathode as the source of lithium since the cathode material usually came in a lithiated form.

This becomes a problem when using the next generation anode and cathode materials in a full cell battery, because when using sulfur as the cathode material for the lithium ion battery, it requires a lithiated form of sulfur. However, lithium sulfide is extremely hazardous, and both lithium sulfide and lithium silicide are air sensitive and require specialized facilities to process and produce.[34-36] To overcome this problem, some has suggested to prelithiated the anode in order to supply lithium to the system, but the methods requires a lot of time and effort.

With sulfur and silicon being the two highest theoretical capacity materials, researchers have also considered to combine sulfur and silicon into a full cell. Such full cell, having a theoretical energy density of 1982 Wh/kg, has three times the theoretical energy density of the existing Li-ion battery system. However, sulfur-silicon full cell is hard to produce due to not only the aforementioned reasons. Researches have been conducted in the field of sulfur silicon full cell, however, researchers have not found a way to avoid prelithiating the silicon or the sulfur electrode. Some researchers such as

Yang et. have chosen to directly work with the prelithiated form of sulfur, which is relatively easier to purchase, but extremely air sensitive and toxic.[34] Some decided to prelithate silicon in lab, by using different methods such as lithiating in electrolyte, applying large pressure, and mixing lithium with the silicon slurry.[35-37] These methods takes up 36 hours, and requires extra equipments since silicon is hard to lithiate, and is unstable once lithiated. Although in these cases the electrodes are prelithiated, and by weight balancing the cathode and anode it should provide enough lithium for the system, the capacity of such batteries is usually around 400-600 mAh/g instead of closer to the theoretical value or the half-cell capacity.[30-33] The major reason is the limited amount of lithium in the system, and solid electrolyte interface using up a great amount of lithium during the first few cycles. This greatly limited the research done on the system, and as a result, researchers have sought alternatives such as trying to make pure lithium foil safe to use as a permanent electrode instead of a temporary testing counter electrode. In this work, a new battery architecture using silicon as the anode and sulfur as the cathode without prelithiation was demonstrated and studied.

Having the same reason as debating if lithium metal should be counted as an anode, there are debates over calling a sulfur-lithium metal battery system a full cell system. A lot have argued that as long as the lithium dendrite formation and corrosion is considered and suppressed, such lithium-sulfur cell should be able to function like any other full cells. Thus, a lot of effort have been put into finding ways to suppress lithium dendrite and lithium corrosion in a lithium-sulfur system. However, when combining lithium metal oxide anode with sulfur cathodes, new complication arises. In one hand,

sulfur batteries use ether-based electrolyte comparing to the usual carbonate-based electrolytes. It is believed that ether-based electrolytes can lead to a more flexible lithium anode sei layer.[38] On the other hand, polysulfides shuttled from the sulfur cathode can form a passivation layer on the lithium anode which greatly affect its sei layer composition and structure.

1.4 Electrochemical characterization techniques for understanding lithium ion batteries

When testing a known battery, researchers often uses a method called conditioning. This method allows for the electrodes in the battery to reach a ready and equilibrium state for future cycling. The importance of this conditioning step was never studied and thus is studied in this work. To do so, galvanostatic cycling with potential limitation (GCPL), cyclic voltammetry (CV), and Electrochemical Impedance Spectroscopy (EIS), and Galvanostatic Intermittent Titration Technique (GITT) are used to test different aspects of the batteries, such as the capacity, resistivity, diffusivity, chemistry, and efficiency. Other than the direct information contained in the data, more information obtained when combining all the data are also analyzed and explained. In this work, all new battery systems and new battery techniques are tested extensively with these characterization methods and the results deeply evaluated.

1.5 References

1. Yin, Ya-Xia, et al. "Lithium–sulfur batteries: electrochemistry, materials, and prospects." *Angewandte Chemie International Edition* 52.50 (2013): 13186-13200.

2. Choi, Nam-Soon, et al. "Challenges facing lithium batteries and electrical double-layer capacitors." *Angewandte Chemie International Edition* 51.40 (2012): 9994-10024.

3. Zhao, Xiaohui, et al. "Lithium/Sulfur SecondaryBatteries: A Review." *Journal of Electrochemical Science and Technology*7 (2016): 97-114.

4. Scrosati, Bruno. "Recent advances in lithium ion battery materials." *Electrochimica Acta* 45.15-16 (2000): 2461-2466.

5. Tarascon, J-M., and Michel Armand. "Issues and challenges facing rechargeable lithium batteries." *Materials For Sustainable Energy: A Collection of Peer-Reviewed Research and Review Articles from Nature Publishing Group*. 2011. 171-179.

6. Lu, Languang, et al. "A review on the key issues for lithium-ion battery management in electric vehicles." *Journal of power sources* 226 (2013): 272-288.

7. Barré, Anthony, et al. "A review on lithium-ion battery ageing mechanisms and estimations for automotive applications." *Journal of Power Sources* 241 (2013): 680-689.

8. Nitta, Naoki, et al. "Li-ion battery materials: present and future." *Materials today* 18.5 (2015): 252-264

9. Su, Xin, et al. "Silicon-based nanomaterials for lithium-ion batteries: a review." *Advanced Energy Materials* 4.1 (2014).

10. Zhang, Wei-Jun. "A review of the electrochemical performance of alloy anodes for lithium-ion batteries." *Journal of Power Sources* 196.1 (2011): 13-24.

11. McDowell, Matthew T., et al. "25th Anniversary Article: Understanding the Lithiation of Silicon and Other Alloying Anodes for Lithium-Ion Batteries." *Advanced Materials* 25.36 (2013): 4966-4985.

12. Liang, Bo, Yanping Liu, and Yunhua Xu. "Silicon-based materials as high capacity anodes for next generation lithium ion batteries." *Journal of Power sources* 267 (2014): 469-490.

13. Chan, Candace K., et al. "Surface chemistry and morphology of the solid electrolyte interphase on silicon nanowire lithium-ion battery anodes." *Journal of Power Sources* 189.2 (2009): 1132-1140.

14. Wu, Hui, et al. "Engineering empty space between Si nanoparticles for lithium-ion battery anodes." *Nano letters* 12.2 (2012): 904-909.

15. Favors, Zachary, et al. "Stable cycling of SiO 2 nanotubes as high-performance anodes for lithium-ion batteries." *Scientific reports* 4 (2014): 4605.

16. Teki, Ranganath, et al. "Nanostructured silicon anodes for lithium ion rechargeable batteries." *Small* 5.20 (2009): 2236-2242.

17. Li, Xiaolin, et al. "Mesoporous silicon sponge as an anti-pulverization structure for high-performance lithium-ion battery anodes." *Nature communications* 5 (2014): 4105.

18. He, Yu, et al. "Alumina-coated patterned amorphous silicon as the anode for a lithium-ion battery with high Coulombic efficiency." *Advanced Materials* 23.42 (2011): 4938-4941.

19. Kim, Hyunjung, et al. "Three-dimensional porous silicon particles for use in high-performance lithium secondary batteries." *Angewandte Chemie* 120.52 (2008): 10305-10308.

20. Li, Changling, et al. "Silicon Derived from glass bottles as anode materials for lithium ion full cell batteries." *Scientific Reports* 7.1 (2017): 917.

21. Yuan, Y. F., et al. "Hierarchically ordered porous nickel oxide array film with enhanced electrochemical properties for lithium ion batteries." *Electrochemistry Communications* 12.7 (2010): 890-893.

22. Yuan, Y. F., et al. "Hierarchically ordered porous nickel oxide array film with enhanced electrochemical properties for lithium ion batteries." *Electrochemistry Communications* 12.7 (2010): 890-893.

23. Cheng, Xin-Bing, et al. "Toward safe lithium metal anode in rechargeable batteries: a review." *Chemical reviews* 117.15 (2017): 10403-10473.

24. Park, Haesun, Hyun Seung Koh, and Donald J. Siegel. "First-Principles Study of Redox End Members in Lithium–Sulfur Batteries." *The Journal of Physical Chemistry C* 119.9 (2015): 4675-4683.

25. Wu, Feixiang, et al. "Lithium iodide as a promising electrolyte additive for lithium–sulfur batteries: mechanisms of performance enhancement." *Advanced Materials* 27.1 (2015): 101-108.

26. Zhang, Sheng S. "Liquid electrolyte lithium/sulfur battery: fundamental chemistry, problems, and solutions." *Journal of Power Sources* 231 (2013): 153-162.

27. Manthiram, Arumugam, Yongzhu Fu, and Yu-Sheng Su. "Challenges and prospects of lithium–sulfur batteries." *Accounts of chemical research* 46.5 (2012): 1125-1134.

28. Canas, Natalia A., et al. "Investigations of lithium–sulfur batteries using electrochemical impedance spectroscopy." *Electrochimica Acta* 97 (2013): 42-51.

29. Pang, Quan, et al. "Advances in lithium–sulfur batteries based on multifunctional cathodes and electrolytes." *Nature Energy*1.9 (2016): 16132.

30. Li, Zhen, Jintao Zhang, and Xiong Wen David Lou. "Hollow carbon nanofibers filled with MnO2 nanosheets as efficient sulfur hosts for lithium–sulfur batteries." *Angewandte Chemie International Edition* 54.44 (2015): 12886-12890.

31. Shan, Jieqiong, et al. "Graphene-directed two-dimensional porous carbon frameworks for high-performance lithium–sulfur battery cathodes." *Journal of Materials Chemistry A* 4.1 (2016): 314-320.

32. Balach, Juan, et al. "Functional Mesoporous Carbon-Coated Separator for Long-Life, High-Energy Lithium–Sulfur Batteries." *Advanced Functional Materials* 25.33 (2015): 5285-5291.

33. Zhang, Liang, et al. "Electronic structure and chemical bonding of a graphene oxide–sulfur nanocomposite for use in superior performance lithium–sulfur cells." *Physical Chemistry Chemical Physics* 14.39 (2012): 13670-13675.

34. Yang, Yuan, et al. "New nanostructured Li2S/silicon rechargeable battery with high specific energy." *Nano letters*10.4 (2010): 1486-1491.

35. Hassoun, Jusef, et al. "A contribution to the progress of high energy batteries: A metal-free, lithium-ion, silicon–sulfur battery." *Journal of Power Sources* 202 (2012): 308-313.

36. Liu, Nian, et al. "Prelithiated silicon nanowires as an anode for lithium ion batteries." *ACS nano* 5.8 (2011): 6487-6493.

37. Weinberger, Manuel, and Margret Wohlfahrt-Mehrens. "Novel strategies towards the realization of larger lithium sulfur/silicon pouch cells." *Electrochimica Acta* 191 (2016): 124-132.

38. Li, Weiyang, et al. "The synergetic effect of lithium polysulfide and lithium nitrate to prevent lithium dendrite growth." *Nature communications* 6 (2015): 7436.

Chapter 2: Free-standing Ni-NiO Nanofiber Cloth Anode for High Capacity, High Rate Li-ion Batteries

2.1 Introduction

Stable high rate, high capacity, and environmentally safe Li-ion battery (LIB) electrodes are at the center of research interest in energy storage.[1–3] LIBs outperform other competing battery technologies currently in the market for portable electronics and are becoming the technology of choice to power next generation electric vehicles.[2,4-7] Research seeks to meet market demands for cost effective, safe, and high performing LIBs through investigating novel materials possessing various nanostructures.[8-10] LIB electrodes often consist of conductive additives, binder, current collector, and active material.[7,11-13] One method of increasing the overall gravimetric capacity of a LIB cell is to eliminate the use of conductive additives and binders in the system. Binders and conductive additives can be replaced by utilizing free-standing electrodes with an embedded current collector. A free-standing electrode incorporates the current collector into the electrode architecture.[14] This reduces the need for the use of binders or conductive additives. However, many of the active materials used are neither conductive enough nor capable of adhering themselves onto the current collector.[4-6] Some free-standing electrodes based on carbon-textile or carbon-based paper**,** carbon-based nano-scaffolds, and electrospun fibers have been shown.[15-18] These exhibit high capacities, fast cycling rates and long cycle lives but suffer from lengthy thermal oxidative stabilization, carbonization, and mechanical fragility.

Candidates for replacement of graphite as an anode - with a theoretical capacity of 372 mAh/g include silicon, tin-based materials, a variety of transition metal oxides, and Li metal.[5-7] These materials exhibit larger capacities than graphite but suffer from potential drawbacks that span from volumetric expansion to poor Coulombic efficiency. Silicon, tin-based materials, and transition metal oxides suffer from volume changes during lithiation/delithiation or from poor conductivity.[7,19] The volume change during cycling causes degradation in the electrode's morphology over the course of its cycle life.[20] As a result, the active material loses contact with the conductive network and the SEI layer degrades. Degradation of the SEI layer results in continual, thicker re-formation of the SEI layer that consumes electrolyte and lithium.[21] Loss of contact with the conductive network and degradation of the SEI layer leads to a decrease in capacity and Coulombic efficiency. Li metal is the ideal material for an anode based on its high capacity, high conductivity, and its lack of need for diffusion/intercalation. The challenges facing Li metal as an anode include repeated formation of Li dendrites during lithiation/delitiation, low Coulombic efficiency, and safety concerns.[21] Metal oxides show promise in alleviating many of the problems faced by next generation Li-ion batteries, but not without the correct electrode design.

Nickel (II) oxide (NiO) is emerging as a promising anode material for high capacity, long cycle life, low cost, and environmentally benign Li-ion batteries.[7] This material system exhibits a high theoretical capacity of 718 mAh/g and an ability to be easily transformed into various 3D structures for use in innovative electrodes.[12] However, the electrochemical performance of NiO is limited by large variations in volume during

lithiation/delithiation and poor conductivity. To combat this issue, various nanostructures have been employed to improve the electrochemical performance such as nanofibers, core-shell nanowires, and carbon structures coated in nickel oxides.[12,22-25] Many of these structures exhibit a long cycle life up to thousands of cycles, exceptional cycling rates up to 10C or high capacities up to 800 mAh/g.[12,26,27] Although these structures have their advantages, none of them combine an outstanding cycle life, high charge current density, and exceptional capacity with a free-standing electrode.

Here we present a novel free-standing Ni-NiO nanofiber cloth anode synthesized by electrospinning and processed by simple heat treatments that address the aforementioned problems. The free-standing Ni-NiO nanofiber cloth anode exhibits a long cycle life of more than 1500 cycles, a high capacity of 1054 mAh/g at a relatively fast cycling rate of 3C (1C=718 mA g^{-1}), and a Coulombic efficiency >99%. Most impressively though, the Ni-NiO fiber cloth anode maintained a high capacity of 1108 mAh/g for more than 1500 cycles at 3C with minimal changes in the morphology post cycling. To the best of our knowledge, an electrospun free-standing Ni-NiO nanofiber cloth anode with a nanostructured metal embedded within the active material serving as the current collector with such outstanding performance has not been previously reported.

2.2 Experimental Details

2.2.1 Material Synthesis

For the preparation of the Ni-NiO fibers, 132 mg mL^{-1} of Ni $(OCOCH_3)_2 \cdot 4H_2O$ and 66 mg mL^{-1} of polyvinylpyrrolidone (PVP, 1 300 000 g mol^{-1}) were mixed in ethanol

for 30 minutes at 70^0C. After the solution was mixed thoroughly, the solution was transferred into a 5 mL syringe and electrospun using the Inovenso Ne300 Nanospinner. The feeding rate of the solution was 0.6 ml hr^{-1} and the spinning potential was 6 kV, while the needle collector distance was 11cm. After the fiber was spun, it was calcined within an Alumina tube at 400^0C for 6 hours in air at a heating rate of 0.66^0C min^{-1} with 2 hours of thermal oxidation stabilization at 200^0C to obtain pure nickel oxide fibers. Thermal oxidation in total took 16h to complete. The nickel oxide fibers were then reduced to nickel fibers by hydrogen reduction at 20 Torr and 400^0C for 90 minutes with a heating rate of 13^0C min^{-1} under a constant flow of Ar/H_2 (1:2 volume ratio). The nickel fibers were cooled down at a cool rate of 20^0C min^{-1}. Lastly, the nickel fibers were re-calcined at 350^0C in air for 30 min with a heating rate of 20^0C min^{-1} to get the Ni core, NiO shell fibers.

2.2.2 Physical Properties Characterization

The morphology of the woven fibers was observed by scanning electron microscopy (Philips XL-30) and transmission electron microscopy (FEI Tecanai12). The synthesized fibers elemental makeup was characterized by X-ray powder diffraction (PANanalytical Empyrean) using Cu-K radiation and EDS (Electron Diffraction Spectroscopy). The makeup of the structure was determined by energy dispersive spectroscopy (Nova NanoSEM 50 Series).

2.2.3 Electrochemical Characterization

Electrochemical measurements were carried out using a type 2032 coin cell with lithium foil acting as the counter electrode and a Celgard 25um 3501 PP separator. The working electrode was prepared by cutting out pieces of Ni-NiO cloth. The resulting cloth was then placed inside the type 2032 coin cell. Assembly of the cells took place in an Argon filled glove box (H_2O < 0.5 ppm, O_2 < 0.2 ppm, VAC). The electrolyte consisted of 1m $LiPF_6$ dissolved in a mixture of Ethylene Carbonate (EC) and dimethyl carbonate (DMC) (1:1 wt.) containing 1% wt. additive of vinyl carbonate (VC). The loading of NiO in the cells was 0.4-0.6 mg cm^{-2} excluding the weight of the nickel core. This loading is calculated by mass-change calculation assuming weight change is only due to oxygen. The type 2032 coin cells were Galvanostatically discharged and charged using an Arbin potentiostat with a voltage range of 0.01-3.0 V vs. Li/Li^+. CV tests were carried out between 0.01-3.0V using a sweep rate of 0.5 mV s^{-1} on an Bio-Logic VMP3. EIS (Bio-Logic VMP3) was carried out at a frequency range that varied from 10 mHz to 100 kHz with an AC signal amplitude of 10 mV. Galvanic cycling, CV, and EIS measurements were all carried out at room temperature (23^0C).

2.3 Results and Discussion

The Ni-NiO fibers were synthesized by electrospinning a sol-gel solution consisting of Nickel acetate ($Ni(CH_3CO_2)_2$) and polyvinylpyrrolidone (PVP) dissolved in ethanol. Oxygen was introduced into the nanofiber structure though calcination at 400^0C in air. The introduction of oxygen results in the formation of nickel oxide (NiO)

nanofibers.[22,28-31] The NiO fibers were reduced at 400^{0}C by hydrogen flow at 20 torr resulting in a dull grey nickel nanofiber cloth. A NiO shell was formed through partial calcination at 350^{0}C in air for half an hour.[32] A detailed schematic of the process is illustrated in Figure 2.1 along with images of the processed materials. Low temperature thermal treatments were utilized in order to keep the grain sizes small. Small grains act as a contributor to facilitate the formation of an advantageous polymer/gel-like coating that forms during cycling.[33,34]

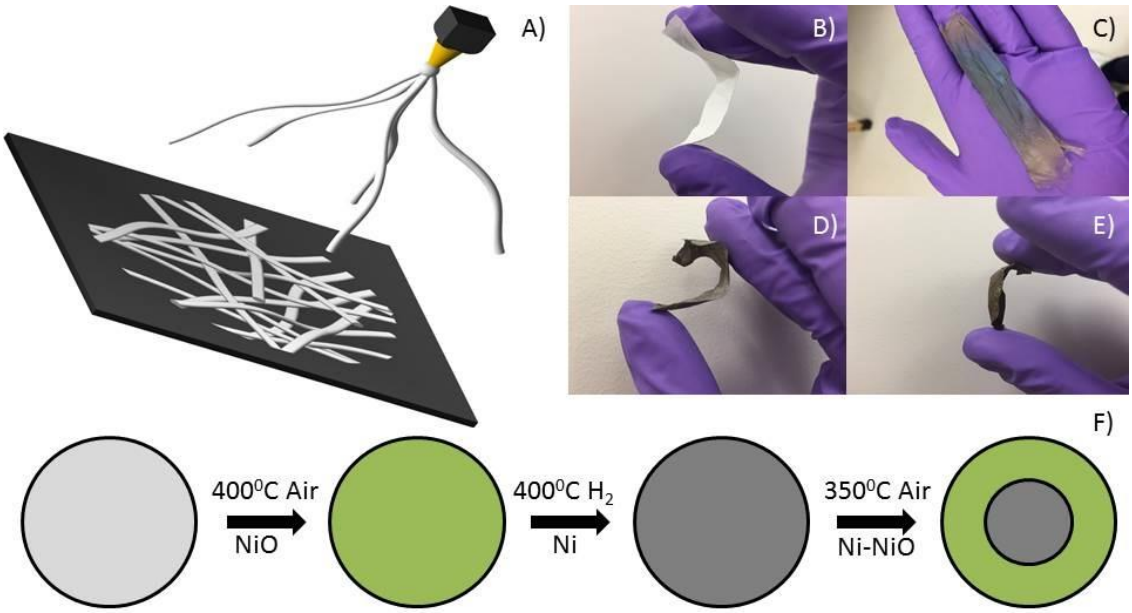

Figure 2.1 A) Electrospinning process. B) As spun nanofiber matte. C) Calcined NiO nanofibers. D) Reduced Ni nanofibers. E) Partially calcined Ni-NiO nanofibers. F) Schematic of the thermal oxidation/reduction process.

Changes in the morphology resulting from thermal treatment were studied using SEM shown in Figure 2.2. The as spun nanofibers in Figure 2.2A show smooth nanofibers with a diameter of approximately 400 nm. Shown in Figure 2.2B, the nanofiber diameter is approximately reduced in half to 200 nm post calcination. This

results from the loss of acetate groups and polymer during thermal treatment. Post hydrogen reduction, the smooth morphology was lost as a result of a volume change from NiO to Ni, shown in Figure 2.2C.[26,27,32] Figure 2.2D shows the formation of a NiO layer on the surface of the Ni nanofibers after partial calcination.

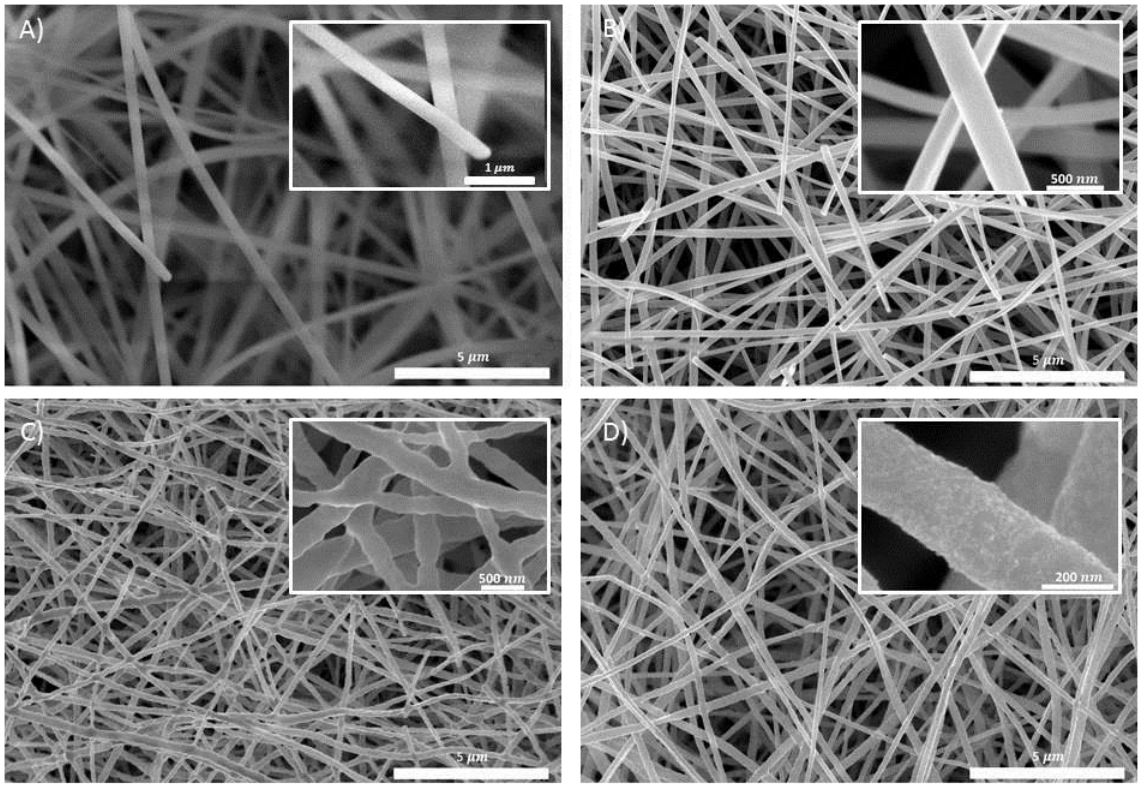

Figure 2.2 A) SEM image of pre-calcined fibers. B) SEM image of NiO fibers post calcination. C) SEM image of Ni fibers post hydrogen reduction. D) SEM image of Ni-NiO fibers with inset image of fibers surface.

The representative Transmission Electron Microscopy (TEM) images shown in Figure 2.3 reveals a distinct oxide layer attributed to nickel oxide on the Ni-NiO fibers, roughly 20 nm in thickness. SAED confirms the presence of an amorphous oxide layer and a crystalline nickel core. The uneven surface morphology of the nickel core results

from the reduction of NiO to Ni. The reduction creates nickel nanocrystals that are tightly bound together, which acts as the backbone of the Ni-NiO cloth fibers. The crystalline nickel and amorphous oxide layer TEM results shown in Figure 2.3 is in agreement with the XRD and EDS results shown in Figure 2.4.

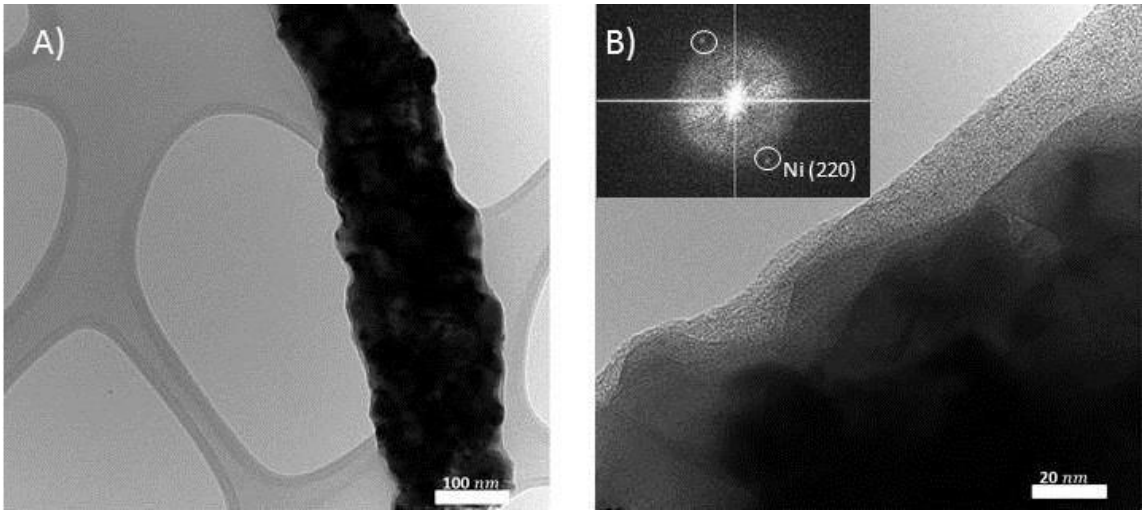

Figure 2.3 A) TEM image of Ni-NiO cloth fiber. B) TEM image of Ni-NiO cloth fiber showing NiO thickness with inset SAED.

The chemical composition of the Ni-NiO nanofibers were confirmed by XRD and EDS. Figure 2.4A shows the XRD pattern of the fibers at different processing phases. The three XRD patterns correspond to NiO, Ni, and Ni-NiO nanofibers post calcination, reduction, and partial-calcination respectively. In Figure 2.4A, the peaks at 37.1°, 43.1° and 62.6° represents the (111), (200), (220) planes of the NiO face-centered cubic crystal structure. The peaks at 44.5°, 51.8° and 76.4°coincides with the XRD pattern for nickel.[35] These peaks correspond to the (111), (200) and (220) planes of the face-centered cubic Ni crystals respectively. The XRD pattern for Ni-NiO nanofibers shows all the peaks from

the previous two XRD patterns. The peaks at 37.1°, 43.1° and 62.6° for NiO are weaker because of the amorphous characteristic, while the peaks at 44.5°, 51.8° and 76.4° are stronger for Ni because of its high crystallinity. No carbon peaks were detected during XRD analysis of the Ni-NiO cloth nano fibers. This shows that the Ni-NiO fibers are only composed of Ni and NiO crystals and all excess carbon was burnt off.[22,36] The XRD results are confirmed by both EDS and TEM shown in Figure 2.4B, Figure 2.3. The EDS spectra in Figure 2.4B show the sole presence of nickel and oxygen within the structure. EDS mapping shows the nickel and oxygen distribution throughout the structure. The distribution of oxygen throughout the structure is represented by the inset image in Figure 2.4C, giving a total of 2.28 wt% oxygen distributed evenly across the surface of the Ni-NiO nanofibers.

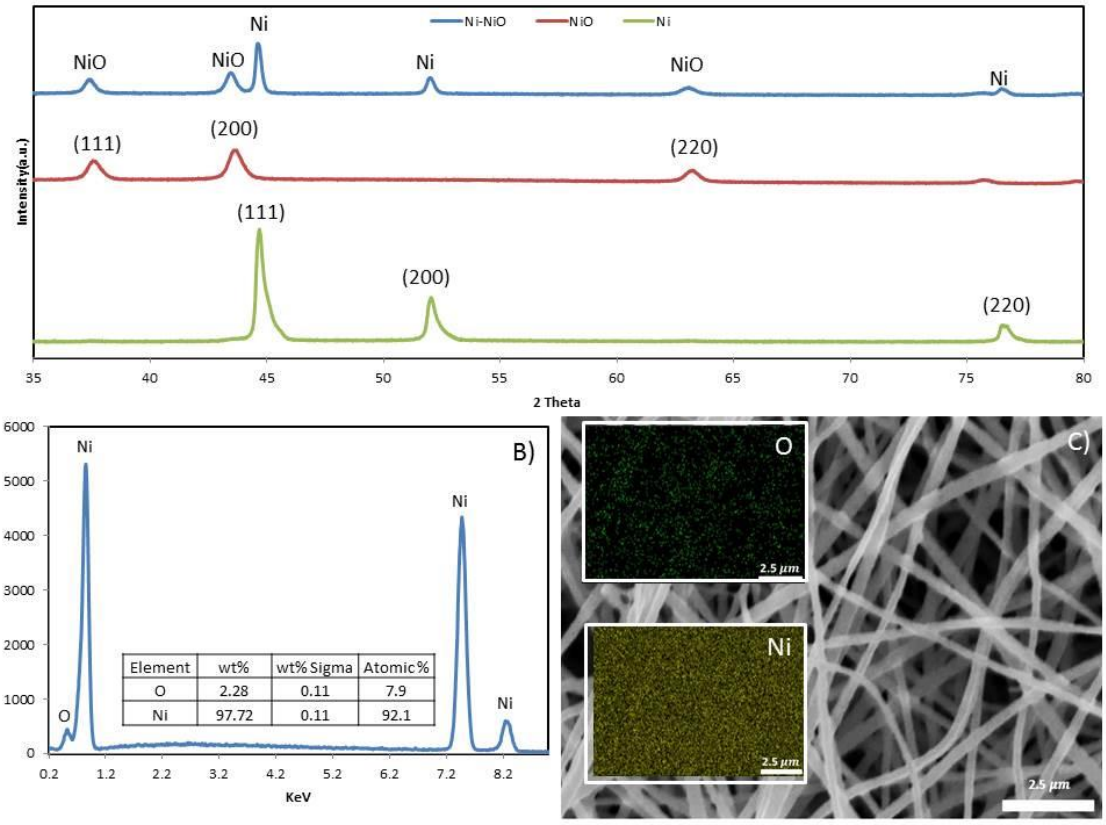

Figure 2.4 A) X-ray powder diffraction of NiO Fibers, Ni Fibers, and Ni-NiO fibers. B) EDS spectra of Ni-NiO fibers with inset display showing weight percentages after partial calcination. C) SEM image of EDS mapped area with inset images of elemental mapping.

The electrochemical properties of the Ni-NiO nanofiber anode was evaluated using galvanostatic cycling, cyclic voltammetry (CV) and electrochemical impedance spectroscopy (EIS). The weight of NiO was calculated by the mass-change measurement, assuming the change mass from pure Ni fibers to partially calcined Ni-NiO fibers are purely due to the introduction of oxygen. The calculated weight was used to determine capacity and C rate. The CV was performed at a scan rate of 0.5 mV s^{-1} over cycles 1-10 and cycles 161-170. Figure 2.5A and Figure 2.5B show the CV profiles for

cycles 1-10, 161-170 respectively. As shown in Figure 2.5A, the CV profile for cycles 2-10 exhibit similar peaks indicating stable cycling performance over the first few cycles.[26] The large difference in the CV profiles for cycles 1 and 2 is most notably the large peak at 0.5 V. The large cathodic peak around 0.5 V is attributed to the formation of the solid electrolyte interface (SEI) layer, the reduction of nickel oxide to nickel, and the formation of amorphous Li_2O ($NiO + 2Li^+ + 2e^- \rightarrow Ni + Li_2O$).[12,26] The cathodic peak at 0.5V is followed by an anodic peak at 2.25V. The anodic peak represents the decomposition of the polymer/gel-like layer and the reversible reduction of Ni^0 to Ni^{2+}. For the remainder of the cycles after the first, the anodic peak shifts to 1 V. The CV profiles for cycles 161-170 is very similar to cycles 2-10 although a current difference exists. The difference in current is attributed to a change in the peak current which alludes to a higher capacity and reactivity.[37] This coincides with the increase in capacity seen after 160 cycles shown in Figure 2.6. The similarities in the curves indicate a very stable cycling performance and the stable formation of the SEI layer after 10 cycles. The stable cycling performance is attributed to the nickel backbone's ability to prevent damage caused by mechanical stress and strain from volume expansion/contraction of 95.68% during lithiation/delithiation of NiO.[38] As a result, the pulverization resistant structure provides a stable conductive network for NiO that is not prone to degradation during lithiation/delithation.[37] This is proven by a constant equivalent series resistance (ESR) of 2.7 for all cycles resulting in an impressive cyclability.

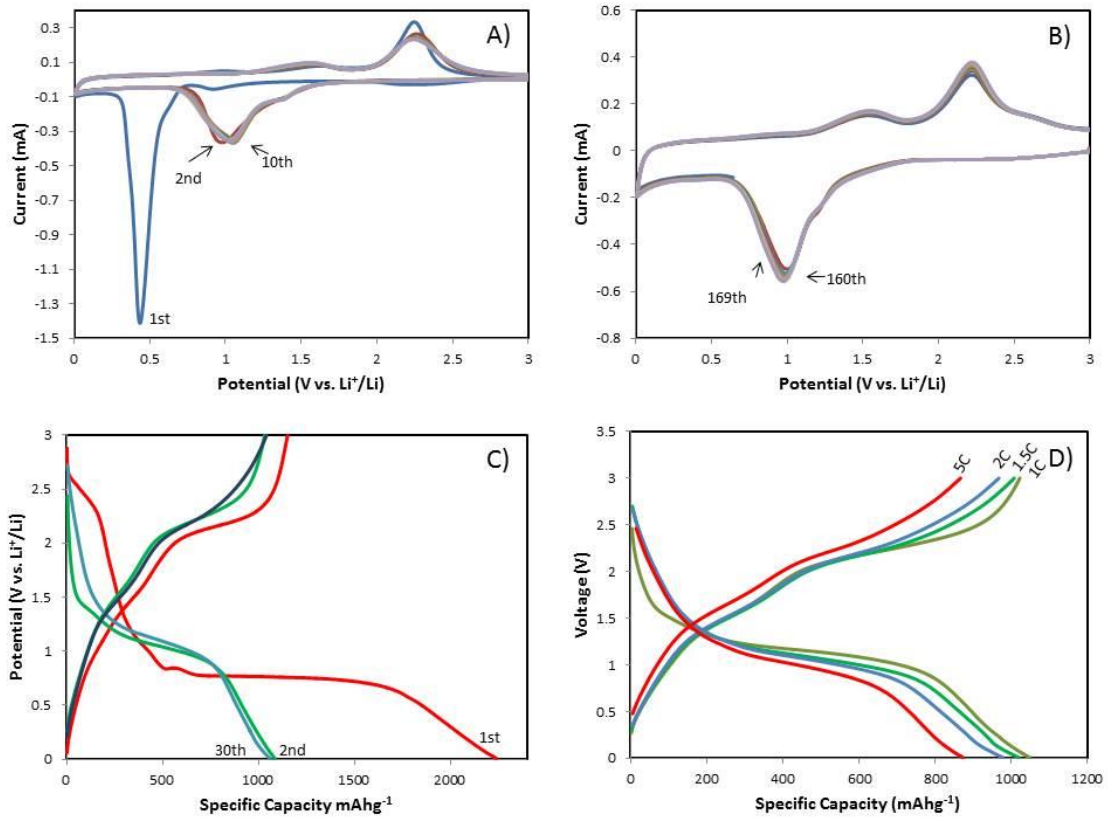

Figure 2.5 A) CV of cycles 1-10 at a scan rate of 0.5 mVs^{-1}. B) CV of cycles 160-169 at a scan rate of 0.5 mVs^{-1}. C) Galvonastic voltage profiles for Ni-NiO fibers at 1C for selected cycles. D) Galvonastic voltage profiles for Ni-NiO fibers at selected C-rates.

The charge-discharge profiles for the Ni-NiO nanofiber electrode between 0.01-3.0V is shown in Figure 2.5. Figure 2.5C shows the charge-discharge profiles at a rate of 1C. The potential of the electrode during its first discharge in Figure 2.5C exhibits a long plateau at 0.85V. The long plateau is attributed to the formation of the SEI layer, initial reduction of NiO to Ni, and the formation of amorphous Li_2O.[12] According to the voltage profile of Figure 2.5C, the polymer/gel like layer starts to form during first discharge cycle around 0.85V, which is usually 0.7V for NiO, and 1.3V for all other cycles. This is

consistent with the CV profiles of NiO reported in literature.[27,32,34,39] The increased voltage plateau from 0.7V to 0.85V for the first cycle results from the eased reaction of NiO with Li^+ to form Ni and Li_2O.[33,34] The main cause of the eased reaction of NiO with Li^+ is the small grain sizes which promote the growth of a polymer/gel-like layer. The polymer/gel-like layer is formed when lithium ions form lithium alkyl carbonate with the electrolyte instead of reacting with the NiO, the lithium alkyl carbonates then build up on the surface of the electrode, forming a polymer/gel like layer.[33] The advantages in the formation of these polymer/gel-like layers are the promotion of a higher capacity and better stability. Firstly, the polymer/gel-like layer causes pseudocapacitance behavior.[33] Psuedocapacitance reactions are known to be highly reversible and to be a source of extra capacity.[33] Secondly, the polymer/gel-like layer holds the active material tightly to the nickel backbone, not only improving the structures conductivity, but also holding the materials tightly together to help maintain its original morphology.[33] As shown in Figure 2.7, the Ni-NiO nanofiber electrode retains its original morphology after 400 cycles at 3C, allowing the electrode to retain a greater portion of its capacity. This polymer/gel like layer remains attached to the surface of the electrode during the remainder of the discharge. During the charge cycle the polymer/gel like layer dissolves when the voltage exceeds 2V contributing to the change in the charge plateau from 2 V to 2.3 V.

The charge-discharge profile for cycles 2 and 30 in Figure 2.5C exhibits similar curves alluding to the stability of the electrode under a cycling rate of 1C. Increasing the cycling rates for the Ni-NiO nanofiber battery results in a higher charge plateau and lower discharge plateau shown in Figure 2.5D. The change in plateaus is a result of a

current density increase, causing a rise in the overpotential of the battery.[26] Despite this, the charge-discharge curves for different cycling rates exhibit similar curves, a plateau between 1.4-0.7V shown in Figure 2.5D. The similarity in the plateaus correlates to the Ni-NiO nanofiber battery's excellent rate performance which is attributed to the rigidity of the nickel as a conductive network during higher cycling rates and the stable formation of the SEI layer. A stable conductive network enhances electrochemical activity by improving electron transport.[40] A stable SEI layer prevents the continual re-formation of a thicker SEI layer which reduces the ionic conductivity and greatly affects the rate capability.[33,41]

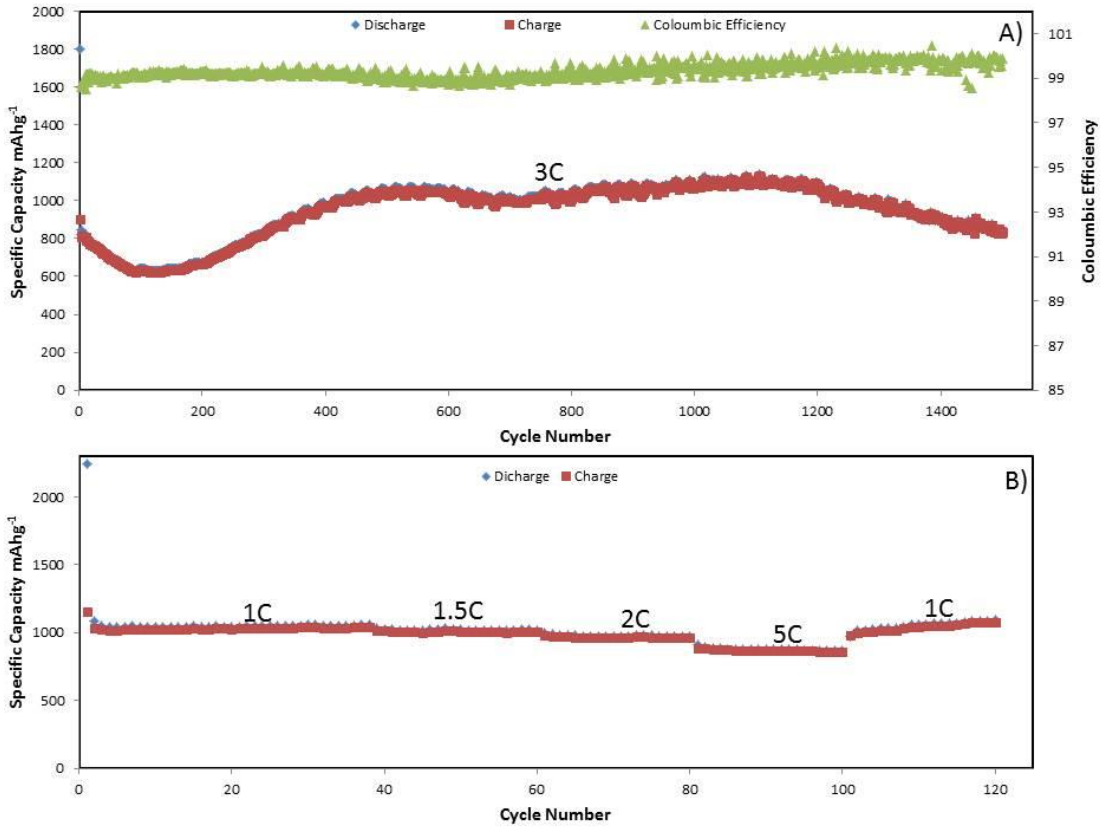

Figure 2.6 A) Deep Galvanostic cycling at 3C for more than 1000 cycles. B) Galvanostic cycling at 1C, 1.5C, 2C, and 5C over 120 cycles.

The Galvanostatic cycling was carried out in the potential window of 0.01 V – 3.0 V using a lithium metal wafer as the counter electrode. As in Figure 2.6A, the capacity was measured at a charging rate of 3C for all cycles. The Ni-NiO batteries show excellent stability and a Coulombic efficiency of >99%. The initial capacity is recorded at 1801 mAh/g, over the next 160 cycles the capacity decreases to 626 mAh/g before increasing again over the next 840 cycles. The decrease in capacity is attributed to the high charge transfer resistance for the first 160 cycles. After 160 cycles, the capacity starts to increase due to a lower charge transfer resistance. This alludes to more of the surface area of the NiO being activated during lithiation/delithiation. The wave like fluctuation in capacity for cycles 100-1000 results from temperature changes occurring inside the room where galvanostatic cycling took place. The increase in capacity over 718 mAh/g can be attributed to a few possible explanations. Do et al. proposed that the increase in capacity results from decreased grain sizes promoting the amount of surface area for nickel oxide to form on the nickel backbone while also promoting the formation of a polymer/gel-like layer.[33,34] Other groups proposed that reversible growth of polymeric/gel-like layers is attributed to the kinetic degradation of the electrolyte.[9,33,34] We attribute the increase in capacity to the nickel backbone acting as an effective catalyst for electrolyte decomposition promoting the continual growth of polymeric/gel-like layers. This results in the battery lasting 1500 cycles while retaining all of its original capacity.

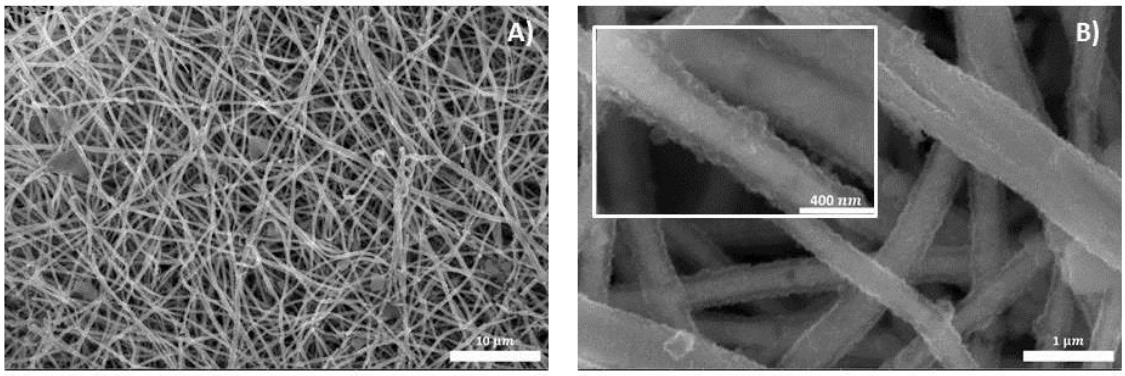

Figure 2.7 A) SEM image post 400 Cycles at 3C. B) SEM image post 400 Cycles at 3C with inset image magnifying fiber structure.

Rate capability is becoming an important factor in next generation LiBs. The rate capability of the Ni-NiO electrode was evaluated over various charge-discharge rates based on the amount of NiO for 120 cycles. Shown in Figure 2.6B, the first cycle exhibits a capacity of 2240 mAh/g and was charged-discharged at a rate of C/10 to ensure proper formation of the SEI layer. At a cycling rate of 718 mA g^{-1}, the Ni-NiO electrode exhibits a capacity of 1084 mAh/g that is well maintained for 60 cycles. Increasing the cycling rate to 1.5C, 2C, 5C for twenty cycles each result in a capacity loss of 2.5%, 6.5%, and 16.2% respectively when compared to the first 60 cycles. Full recovery of the original capacity is achieved when the cycling rate is returned to 1C. The Ni-NiO excellent rate capability is attributed to the stability of the electrode architecture under higher current densities, which maintains the conductivity of the system. Post cycling images in Figure 2.7 confirm the ability of Ni-NiO to maintain its initial morphology after 400 cycles at 3C, showing very little to no degradation. These results show that the free-standing Ni-NiO nanofiber, compared to that of a slurry cast electrode, has a longer life, a higher capacity, a better stability, and a better rate capability without damaging the

electrode. This is due to the elimination of binders and conductive additives that would otherwise reduce the overall gravimetric capacity and the formation of a stable SEI layer that would otherwise reduce ionic conductivity.

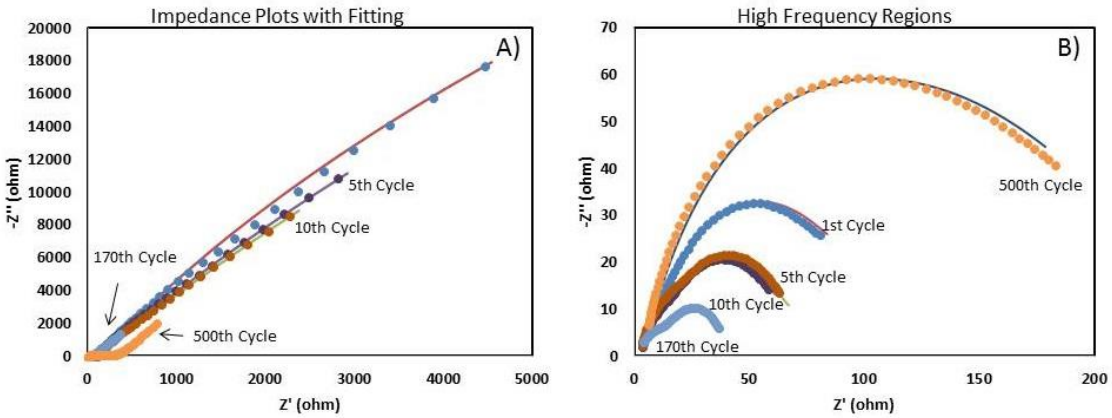

Figure 2.8 A) Complex impedance plots of Ni-NiO nanofiber anode for selected cycles. B) High frequency regions of plots.

Complex impedance plots for the first ten cycles, near 170 cycles, and near 500 cycles were obtained by running potentiostatic electrochemical impedance spectroscopy (PEIS). Electrochemical impedance spectroscopy (EIS) is a technique that applies a small sinusoidal of varying frequency and measures the resultant complex impedance. For the current investigation, 10 mV sinusoidal signals with frequencies ranging from 10 mHz to 100 kHz were applied. The plots contain the following distinct features: a high frequency intercept, two curves resembling semicircles at the higher frequency end, and a low frequency tail.[42] Figure 2.8A shows complex impedance plots for selected cycles and their model fits in accordance with the impedance of the electrical equivalent circuit shown in Figure 2.9. The high frequency intercepts represent electronic resistance in

conductive material within the electrode in combination with the ionic resistance of the electrolyte, often presented as the equivalent series resistance (ESR). The Ni-NiO anode has a comparatively low ESR. More remarkably, this Ohmic resistance does not increase with cycling but stays at its initial value throughout 170 cycles, as shown in Table 1. This supports the claim that the nickel backbone provides a robust conductive network for the Ni-NiO anode that can withstand volume change during lithiation/delithiation without deterioration. Another thing to notice is the slight mismatch in fitting for the first cycle seen in Figure 2.8B. The equivalent circuit is composed of modeled parameters design to predict electrochemistry within a LIB cell. While the cell behavior becomes more predictable during later cycles, it may sometimes show evidence electrochemical steps that only are present during the first cycle (not represented in the equivalent circuit model).

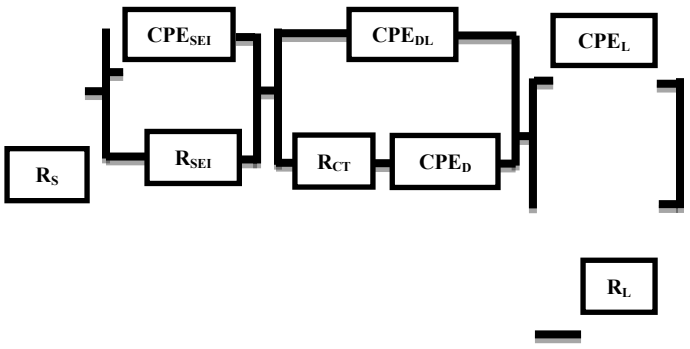

Figure 2.9 Electrical equivalent circuit used for fitting the complex impedance plots.

A low and stable value for ESR is indicative of excellent rate capabilities as observed during Galvanostic cycling. The first semicircle shape represents a frequency dependent complex impedance of the solid-electrolyte interphase that forms on the surface of the active material due to irreversible reactions involving lithium ions and solvent molecules. The diameter of the semicircle represents the resistance due to the solid-electrolyte interphase (SEI) layer, listed here as R_{SEI}.[43] The second semicircle contains impedance information on the electrochemical double layer that forms at the electrode-electrolyte interface.[44] The reaction kinetics that allows a battery to store energy takes place in this electrochemically active region. The diameter of this semicircle represents charge-transfer resistance or reaction resistance (R_{CT}) for the redox reactions involved in lithium ion exchange at the electrode.

Table 2.1 Lists relevant parameters obtained from EIS analysis of Ni-NiO anode.

Cycle	ESR	Rsei	Rct
1	**2.7**	**5**	**88**
2	**2.7**	**7.5**	**65**
3	**2.7**	**7.5**	**62**
4	**2.7**	**8**	**60**
5	**2.7**	**9**	**53**
10	**2.7**	**10**	**56**
170	**2.7**	**10**	**27**
501	**3.5**	**60**	**150**

Table 1 shows the evolution of R_{SEI} and R_{CT} with cycling for our Ni-NiO anode. The SEI resistance increases during the initial ten cycles while the electrochemically inert layer formed on active material surface. R_{SEI} stabilizes thereafter and maintains the same value through 170 cycles. Stable formation of the SEI layer is mandatory for good rate capabilities and cycling stability and is coherent in light of the excellent cycle life demonstrated in Figure 2.6B.[45] The sharp increase in SEI observed after 500 cycles may be due to the desolvation of gel/polymer layer formed on NiO surface, which led to new SEI formation. The R_{CT} decreases sharply during the initial cycles and continues to decrease through 170 cycles. The R_{CT} is expected to decrease with cycling in a high surface-area electrode, as more of the active material surface is activated via repeated lithiation/delithiation of the electrode. The results of EIS confirm the crucial role of the nickel backbone in enhancing the stability of the free-standing Ni-NIO cloth anode and the stable formation of the SEI layer.

2.4 Conclusion

In summary, we have presented here a novel free-standing Ni-NiO cloth anode synthesized by electrospinning followed by thermal oxidation/reduction processes. As an anode material for next generation LIBs, the free-standing Ni-NiO cloth anode exhibits an outstanding high capacity of 1054 mAh/g, a long-life of 1000 Cycles at 3C or 2154 mA g^{-1}, and an great rate capability up to 5C or 3590 mA g^{-1}. This work demonstrates a facile approach for achieving impressive performance using Ni-NiO cloth as an anode. The results presented here show that the free-standing Ni-NiO cloth electrode is capable

of replacing graphite anodes and providing the performance needed in LiBs for the next generation of portable and flexible electronics.

2.5 References

1. Deng, Da, et al. "Green energy storage materials: Nanostructured TiO 2 and Sn-based anodes for lithium-ion batteries." Energy & Environmental Science 2.8 (2009): 818-837.

2. Armand, Michel, and J-M. Tarascon. "Building better batteries." nature 451.7179 (2008): 652.

3. Xu, Gui-Liang, et al. "Synthesis of Co3O4 nano-octahedra enclosed by {111} facets and their excellent lithium storage properties as anode material of lithium ion batteries." Nano Energy 2.3 (2013): 394-402.

4. Etacheri, Vinodkumar, et al. "Challenges in the development of advanced Li-ion batteries: a review." Energy & Environmental Science 4.9 (2011): 3243-3262.

5. Choi, Nam-Soon, et al. "Challenges facing lithium batteries and electrical double-layer capacitors." Angewandte Chemie International Edition 51.40 (2012): 9994-10024.

6. Goodenough, John B., and Youngsik Kim. "Challenges for rechargeable Li batteries." Chemistry of materials 22.3 (2009): 587-603.

7. Reddy, M. V., G. V. Subba Rao, and B. V. R. Chowdari. "Metal oxides and oxysalts as anode materials for Li ion batteries." Chemical reviews 113.7 (2013): 5364-5457.

8. Xu, Jiantie, et al. "Cathode materials for next generation lithium ion batteries." Nano Energy 2.4 (2013): 439-442.

9. Zhang, Wei-Jun. "A review of the electrochemical performance of alloy anodes for lithium-ion batteries." Journal of Power Sources 196.1 (2011): 13-24.

10. Mukherjee, Rahul, et al. "Nanostructured electrodes for high-power lithium ion batteries." Nano Energy 1.4 (2012): 518-533.

11. Cabanas-Polo, S., et al. "Cyclability of binder-free β-Ni (OH) 2 anodes shaped by EPD for Li-ion batteries." Journal of the European Ceramic Society 35.2 (2015): 573-584.

12. Kawamori, Makoto, et al. "Three-dimensional nanoelectrode by metal nanowire nonwoven clothes." Nano letters 14.4 (2014): 1932-1937.

13. Li, Xifei, et al. "Binder-free porous core–shell structured Ni/NiO configuration for application of high performance lithium ion batteries." Electrochemistry Communications 12.9 (2010): 1222-1225.

14. Lee, Sang-Young, et al. "Progress in flexible energy storage and conversion systems, with a focus on cable-type lithium-ion batteries." Energy & Environmental Science 6.8 (2013): 2414-2423.

15. Balogun, Muhammad-Sadeeq, et al. "Binder-free Fe2N nanoparticles on carbon textile with high power density as novel anode for high-performance flexible lithium ion batteries." Nano Energy 11 (2015): 348-355.

16. Chen, Minghua, et al. "Porous α-Fe2O3 nanorods supported on carbon nanotubes-graphene foam as superior anode for lithium ion batteries." Nano Energy 9 (2014): 364-372.

17. Zhu, Lin, et al. "Interconnected carbon nanotube/graphene nanosphere scaffolds as free-standing paper electrode for high-rate and ultra-stable lithium–sulfur batteries." Nano Energy 11 (2015): 746-755.

18. Hwang, Tae Hoon, et al. "Electrospun core–shell fibers for robust silicon nanoparticle-based lithium ion battery anodes." Nano letters 12.2 (2012): 802-807.

19. Liu, Yongfeng, et al. "Cycling durability and degradation behavior of La–Mg–Ni–Co-type metal hydride electrodes." Journal of Alloys and Compounds 395.1-2 (2005): 291-299.

20. Poizot, P. L. S. G., et al. "Nano-sized transition-metal oxides as negative-electrode materials for lithium-ion batteries." Nature 407.6803 (2000): 496.

21. Xu, Wu, et al. "Lithium metal anodes for rechargeable batteries." Energy & Environmental Science 7.2 (2014): 513-537.

22. Aravindan, Vanchiappan, et al. "Electrospun NiO nanofibers as high performance anode material for Li-ion batteries." Journal of Power Sources 227 (2013): 284-290.

23. Wang, Bin, et al. "Electrochemical performance of carbon/Ni composite fibers from electrospinning as anode material for lithium ion batteries." Journal of Materials Chemistry A 1.4 (2013): 1368-1373.

24. An, Zhonglie, et al. "Microstructuring of carbon nanotubes-nickel nanocomposite." Nanotechnology 26.19 (2015): 195601.

25. Luo, Chenghao, et al. "Preparation of C/Ni–NiO composite nanofibers for anode materials in lithium-ion batteries." Applied Physics A 113.3 (2013): 683-692.

26. Sun, X., et al. "Adv. Energy Mater. 4 (2014)."

27. Sun, Xiaolei, et al. "Multifunctional Ni/NiO hybrid nanomembranes as anode materials for high-rate Li-ion batteries." Nano Energy 9 (2014): 168-175.

28. Barakat, Nasser AM, Bongsoo Kim, and Hak Yong Kim. "Production of smooth and pure nickel metal nanofibers by the electrospinning technique: nanofibers possess splendid magnetic properties." The Journal of Physical Chemistry C113.2 (2008): 531-536.

29. Kim, Chan, et al. "Fabrication of electrospinning-derived carbon nanofiber webs for the anode material of lithium-ion secondary batteries." Advanced functional materials 16.18 (2006): 2393-2397.

30. Teo, Wee E., and Seeram Ramakrishna. "A review on electrospinning design and nanofibre assemblies." Nanotechnology 17.14 (2006): R89.

31. Wu, Hui, et al. "Electrospinning of Fe, Co, and Ni nanofibers: synthesis, assembly, and magnetic properties." Chemistry of materials 19.14 (2007): 3506-3511.

32. Wang, Xinghui, et al. "Nanostructured NiO electrode for high rate Li-ion batteries." Journal of Materials Chemistry 21.11 (2011): 3571-3573.

33. Laruelle, S., et al. "On the origin of the extra electrochemical capacity displayed by MO/Li cells at low potential." Journal of the Electrochemical Society 149.5 (2002): A627-A634.

34. Do, Jing-Shan, and Chien-Hsiang Weng. "Preparation and characterization of CoO used as anodic material of lithium battery." Journal of power sources 146.1-2 (2005): 482-486.

35. Needham, Scott A., G. X. Wang, and Hua-Kun Liu. "Synthesis of NiO nanotubes for use as negative electrodes in lithium ion batteries." Journal of Power Sources 159.1 (2006): 254-257.

36. Li, Tao, et al. "Preparation of NiO–Ni/natural graphite composite anode for lithium ion batteries." Journal of Alloys and Compounds 553 (2013): 167-171.

37. Su, Liwei, Zhen Zhou, and Panwen Shen. "Ni/C hierarchical nanostructures with Ni nanoparticles highly dispersed in N-containing carbon nanosheets: origin of Li

storage capacity." The Journal of Physical Chemistry C 116.45 (2012): 23974-23980.

38. Su, Dawei, Mike Ford, and Guoxiu Wang. "Mesoporous NiO crystals with dominantly exposed {110} reactive facets for ultrafast lithium storage." Scientific reports 2 (2012): 924.

39. Li, Xifei, Abirami Dhanabalan, and Chunlei Wang. "Enhanced electrochemical performance of porous NiO–Ni nanocomposite anode for lithium ion batteries." Journal of Power Sources 196.22 (2011): 9625-9630.

40. Li, Dan, et al. "Building a Ni 3 S 2 nanotube array and investigating its application as an electrode for lithium ion batteries." Chemical Communications 50.66 (2014): 9361-9364.

41. Ogihara, Nobuhiro, et al. "Disordered carbon negative electrode for electrochemical capacitors and high-rate batteries." Electrochimica acta 52.4 (2006): 1713-1720.

42. Favors, Zachary, et al. "Scalable synthesis of nano-silicon from beach sand for long cycle life Li-ion batteries." Scientific reports 4 (2014): 5623.

43. Zhang, S. S., K. Xu, and T. R. Jow. "Electrochemical impedance study on the low temperature of Li-ion batteries." Electrochimica acta 49.7 (2004): 1057-1061.

44. Wang, Wei, et al. "Silicon decorated cone shaped carbon nanotube clusters for lithium ion battery anodes." Small 10.16 (2014): 3389-3396.

45. P. Verma, P. Maire, P. Novák, Electrochim. Acta 55 (2010) 6332-6341

Chapter 3: Advanced Sulfur-Silicon Full Cell Architecture for Lithium Ion Batteries

3.1 Introduction

Lithium-ion batteries (LiBs) outperform other battery technologies on the market, making them the choice for consumer electronics and electric vehicles (EVs). However, performance and cost demands have begun exceeding the capabilities of current LiB technology. Researchers have turned towards next generation battery materials to procure cheaper, higher capacity batteries.[1-7]

Current LiBs utilize a cathode made from lithiated metal oxides, such as lithium nickel manganese cobalt oxide (NMC). The cathode is traditionally countered by a graphite anode, although some in the industry have recently started incorporating silicon into the anode (1%-5%). The advantages to this combination are high rate capabilities, low capacity degradation, and long lifetime. The disadvantages are a limited energy density, with NMC/Graphite having the highest theoretical energy density at 605 Wh/kg, and high cost of $180/kWh. To reduce costs, researchers have turned toward more energy dense and cheaper materials.

Sulfur is an attractive cathode material due to its theoretical capacity of 1675 mAh/g. However, implementation of sulfur has been slow due to its inherent problems including polysulfide shuttling, volumetric expansion, and poor conductivity.[1,2,8-11] Polysulfide shuttling results from higher order polysulfides dissolving in the electrolyte, causing long term capacity degradation and slowing reaction kinetics during runtime.[12] Volumetric expansion results from sulfur expanding (80%) during lithiation/delithiation

which causes mechanical degradation to the electrode's conductive network.[12] Finally, sulfur's insulating properties affect the electrode's rate capabilities. Fortunately, researchers have discovered methods to alleviate these issues ranging from mechanical barriers, to porous carbon networks, to other chemical methods.[13-17] Promising performance from these solutions have resulted in much fervor surrounding sulfur.

The current anode of choice is silicon for its high theoretical capacity of 4200 mAh/g. Silicon faces two challenges - poor conductivity, and volumetric expansion.[18-21] During lithiation/delithiation, silicon's volume changes 400% which mechanically pulverizes the electrode, and degrades its cycle life and rate capabilities.[21,22] To alleviate these issues, researchers utilize novel methods including nano silicon structures, conductive additives, and binders.[23-29] Ultimately, the immense focus on solving each electrode's issues has resulted in less research effort on combining a sulfur cathode and silicon anode in a full-cell configuration.

A full cell using sulfur and silicon electrodes is attractive for several reasons. Sulfur and silicon are environmentally benign and abundant. Furthermore, theoretical energy density of a sulfur silicon full-cell (SSFCs) is 1982 Wh/kg, far exceeding the theoretical energy density of current LiBs while only potentially costing $13/kWh. However, a major restriction for SSFCs is the lithium source. Currently, researchers utilize pre-lithiated materials such as lithium sulfide or lithium silicide, allowing for energy densities up to 600 Wh/kg. However,these full cells suffer from short cycles lives, typically less than 50 cycles, while the material used require specialized equipment and face restrictions in processing.[30-32]

Here, we present an advanced LiB architecture utilizing a sulfur cathode and silicon anode with lithium source integrated into the Si anode that can bypass these issues. The SSFC exhibits an energy density of 350 Wh/kg for 260 cycles at C/10. To the best of our knowledge, an SSFC with this architecture has not been reported.

3.2 Experimental Details

3.2.1 Material Synthesis

The SSFCs consist of a sulfur cathode and a silicon anode. The sulfur cathode was made with 20 wt% Poly(acrylic acid) (PAA, 1800 g/mol,Sigma-Aldrich) and 80% wt% acetylene black sulfur composite(ABS). The aforementioned ABS was made by dissolving 200 mg of Sulfur (S, 99.998% trace metals basis, Sigma-Aldrich) in 20 ml of Dimethyl Sulfoxide (DMSO, Fisher Chemical) at 90 C, heated by a heating jacket (Brisk Heat). 129 mg of Acetylene black (Alfa aesar, 50% compressed) was then added to the solution, the solution was stirred for 3 hours before the heating jacket was removed and the solution was allowed to cool while stirring. The resulting ABS composite was then washed by anhydrous ethanol (Decon Labs, Inc.) several times to ensure the removal of DMSO and dried at 60C for 24 hours. To make the sulfur electrode, Poly(acrylic acid) (Sigma Aldrich, 450,000) and ABS were mixed with 1-Methyl-2-pyrrolidinone (NMP, Sigma-Aldrich) and then casted on a large piece of aluminum chip (Alfa Aesar, 0.025mm thickness, 99.45% purity) by a doctor blade (MTI Automatic Thick Film Coater, BYK Doctor Blade). The casted electrode sheet was then dried in a convection oven (Cole-Parmer, Stable Temp) at 60C for 24 hours. The silicon electrode was made with 40 wt%

of commercial silicon (GNM Silicon nanoparticles 80nm), 25 wt% Acetylene black (Alfa aesar, 50% compressed), and 35 wt% Poly (acrylic acid) (Sigma Aldrich, 450,000). The materials were mixed and sonicated in ethanol and then casted on a large copper chip (Alfa Aesar, 0.025mm thickness, 99.8% purity) with a doctor blade (BYK) and was then dried at 60C for 24 hours**.** Both electrodes were calendared with a 0.04 mm calendar gap using a calendaring machine (IRM) before being constructed into a coin cell.

3.2.2 Physical Characterization

The morphology of the electrode pre and post cycling was observed by scanning electron microscopy (NovaNanoSEM 450)

3.2.3 Electrochemical Characterization

To make the SSFC battery, a silicon electrode (16mm in diameter) was first put inside a negative cap (MTI type 2032 coin cell case) and a piece of lithium (MTI Lithium Chip 15.6 Dia x 0.25t mm) with corresponding weight (4-6 mg depending on electrode weight, with adjustments for SEI consumption) was adhered to the top of the silicon electrode inside an Ar filled glovebox (H_2O < 0.5 ppm, O_2 < 0.2 ppm, Vacuum Atmosphere Co.) to form a complete circuit. The amount of lithium needed was calculated based on the electrode weights and SEI lithium consumption of the half-cells. Next, separators (Celgard 25um 3501) of various sizes were placed on top to prevent any possibility of shorting. Sulfur electrode (16mm in diameter) was then placed on top followed by two spacers, a spring, and the positive cap were added with the electrolyte in

between (1:1 DOL:DME, 1wt%$LiNO_3$, 1M LiTFSI). The battery was then sealed using a battery crimper (MTI, MSK-160D). The battery was tested under room temperature with a Bio Logic (BCS 810 Testing Module) using different testing methods, including Galvanostatic Cycling with Potential Limitation (GCPL), Cyclic Voltammetry (CV), Potentiostatic Electrochemical Impedance Spectroscopy (PEIS) and Galvanostatic Intermittent Titration Technique (GITT) in voltage window ranging from 1.5V to 2.6V. The same tests were also performed for the sulfur half-cell (between 1.7V to 2.8V) and the silicon half-cell (between 0.01V to 1V). The Sulfur weight percentage in the Acetylene Black Sulfur composite (ABS) was measured using thermogravimetric analysis (TGA), showing 57% weight sulfur. The SSFC and sulfur half-cell were conditioned with a current rate of 0.175 mA (C/50) and cycled at 0.875 mA (C/10). The silicon half-cell was conditioned at a current rate of 0.336mA (C/50) and cycled at 1.68 mA (C/10).

3.3 Results and Discussion

Electrodes for SSFCs were constructed using a facile process. Shown in Figure 3.1A, the silicon electrode is patterned to create an access point for the lithium chip, sitting on top of the silicon electrode, to contact the current collector. The access point allows electrons to transfer from lithium to positive terminal, Figure 3.1C, creating a complete circuit. During discharge, the surface area of the lithium chip with direct access to the outer circuit alongside with the silicon anode should act as a lithium source. This provides lithium ions to the cathode through electrolyte while electrons travel to the

cathode through the outer circuit. During charge, due to the reducing property of lithium, lithium ions will preferentially react with the silicon anode instead of the lithium chip. As cycling increases, lithium without direct access to the outer circuit also integrates into the system. This results in an increase in capacity, discussed later in Figure 3.5C. Each SSFC requires roughly 6.44 mg of lithium, accounting for the lithiation of sulfur and silicon, along with consumption of lithium by the SEI. (See supplementary document for detailed calculation) To ensure enough lithium is available in the system, each cell is loaded with 8 mg of lithium.

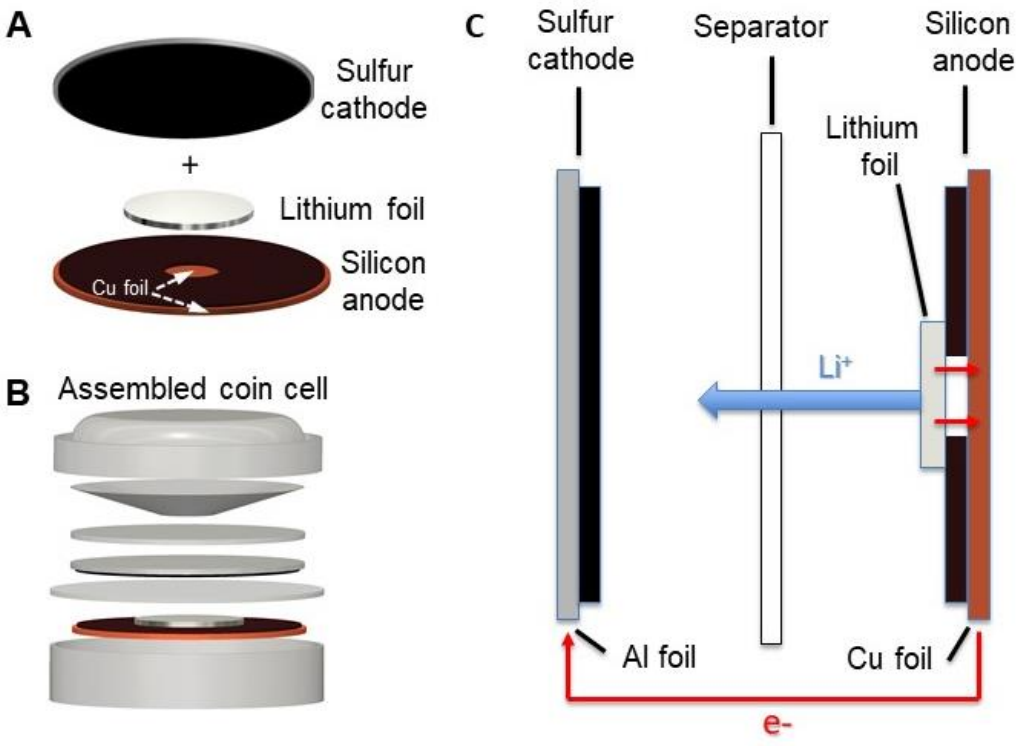

Figure 3.1 A) SSFC battery architecture set up. B) Assembled SSFC coin cell schematic. C) SSFC Cross sectional discharge schematic.

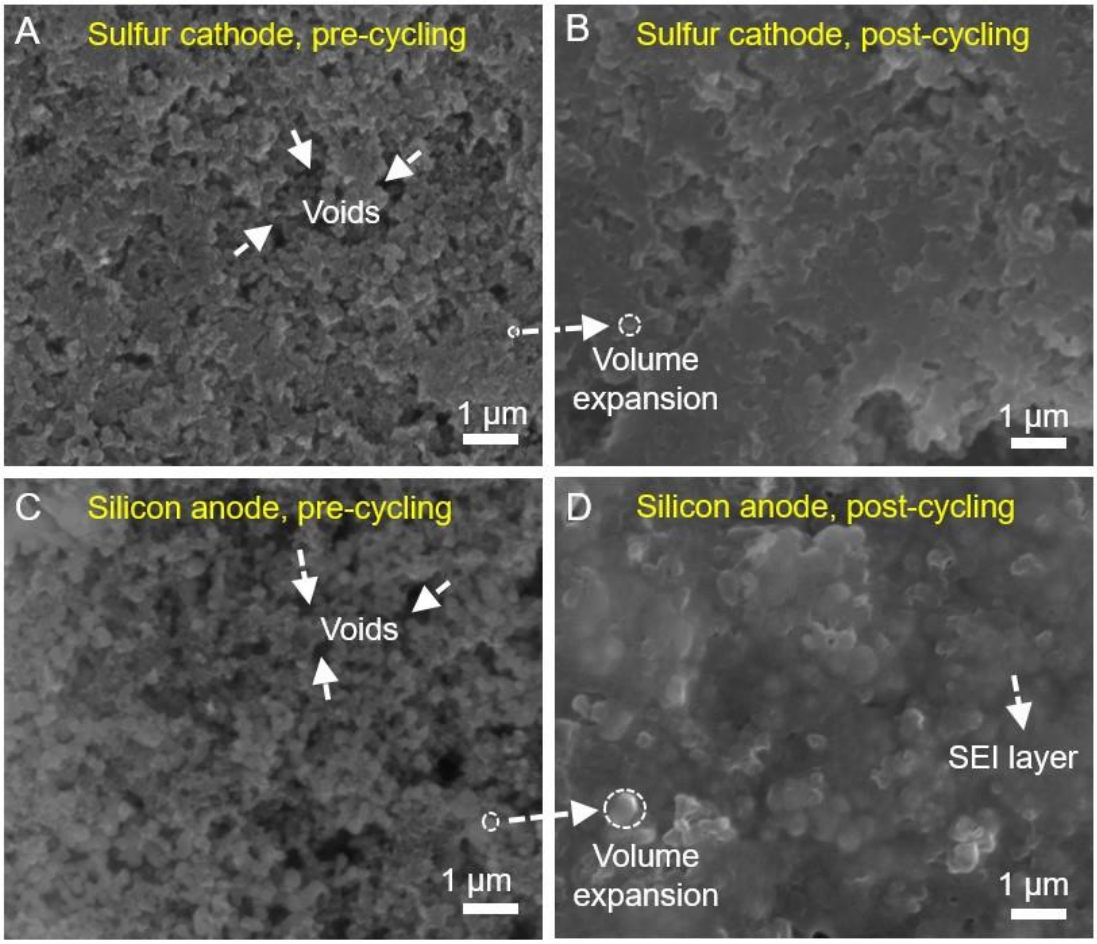

Figure 3.2 SEM images of sulfur cathode (A, B) and silicon anode (C, D) before and after 300 charge/discharge cycles, respectively.

The morphology of the electrodes was examined using SEM, shown in Figure 3.2. Figure 3.2A and 3.2C show the surface of the sulfur and silicon electrodes respectively before they were cycled in the SSFC. Figure 3.2B and 3.2D show the post-cycling morphology of the corresponding electrodes. Pre-cycling SEM shows the electrode materials are loosely packed with large void spaces existing after calendaring. Post-

cycling SEM shows less void space due to the volumetric expansion of active materials and the formation of SEI products during lithiation.[3,18] The post-cycling SEM of the lithium foil after 310 cycles was also done to further confirm that silicon is being used as the anode.

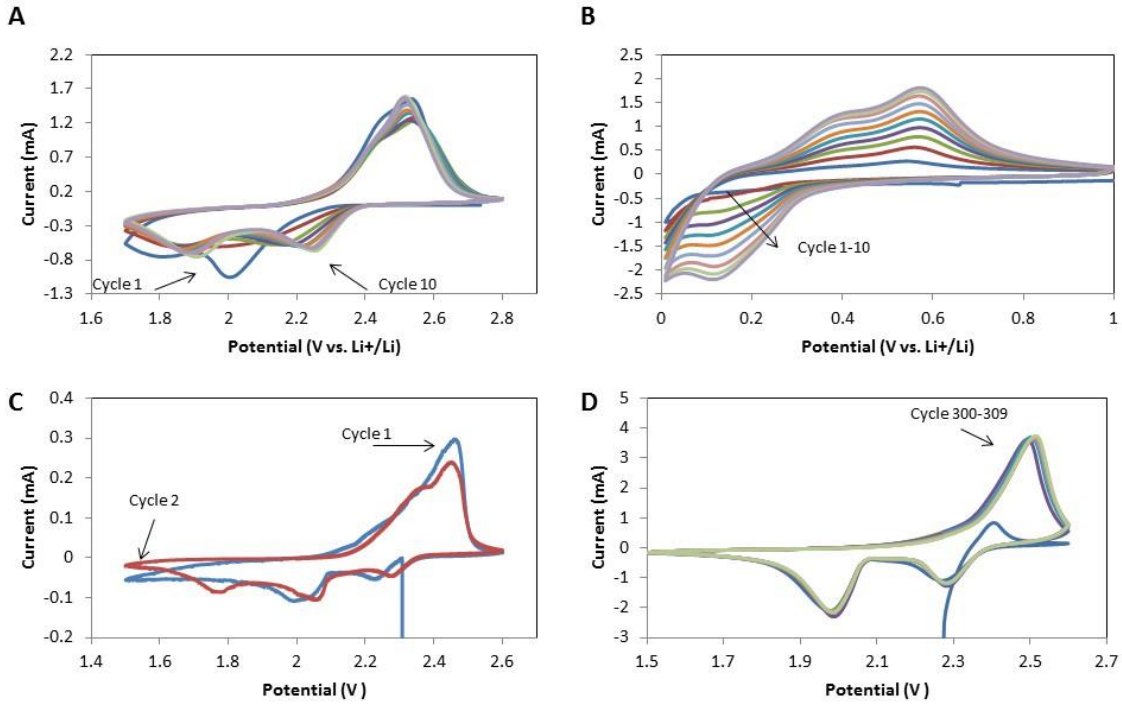

Figure 3.3 A) Cycles 1-10 for the sulfur electrode at a scan rate of 0.1 mVs^{-1}. B) Cycles 1-10 for the silicon electrode at a scan rate of 0.1 mVs^{-1}. C) CV of Cycles 1-2 for the SSFC at a scan rate of 0.05 mVs^{-1}. D) CV of Cycles 300-309 for the SSFC at a scan rate of 0.1 mVs^{-1}.

CV was performed at a scan rate of 0.1 mV s^{-1} over cycles 1-10 for both sulfur and silicon half-cells. SSFC CV was conducted at 0.05 mV s^{-1} and 0.1 mV s^{-1} respectively for cycles 1-2 and 300-309. The 0.05 mV s^{-1} scan rate was used to

accommodate the aforementioned requirements for lithium integration during cycles 1-2. Figures 3.3A and 3B show CV profiles for cycles 1-10 of sulfur and silicon half-cells respectively. Shown in Figure 3.3A, the sulfur half-cell exhibits typical characteristics of chemical reactions between sulfur and lithium ions with two cathodic peaks at 1.9 V and 2.25 V followed by an anodic peak at around 2.5 V.[33,34] The notable difference for cycles 1 and 2 is the offset peaks at 1.8 V and 2 V. Peaks shifting towards a higher potential indicates a higher ionic conductivity stemming from increased polysulfides and SEI formation.[35] Shown in Figure 3.3B, the silicon half-cell shows typical cathodic peaks at 0.18 V and 0.1 V with anodic peaks at 0.4 V and 0.6 V. The cathodic and anodic peaks corresponding to lithiation/delithiation increase in intensity over time, resulting from lithiation of the native SiO_2 layer and lithium gaining access to additional silicon.[36] The peak associated with SEI formation (0.67 V) does not exist after the first cycle, showing bulk SEI formation has been achieved.[36]

Figures 3.3C and 3.3D show CV profiles for the SSFC for cycles 1-2 and 300-309 respectively. Figures 3.3C and 3.3D exhibit a similar electrochemistry to Figure 3.3A resulting from interactions between lithium ions and sulfur dominating the SSFC chemistry. In Figure 3.3C, the first cycle has cathodic peaks at 2 V and 2.2 V resulting from limited amounts of lithium participating in the first discharge. Cycle two has an additional peak around 1.8 V, which we hypothesize to be a result of the negative voltage potential between the non-participating lithium and silicon. The resulting equilibrium voltage equals to the difference between the original potential of unlithiated sulfur and lithium (~2.8 V), and the potential between silicon and lithium (~1V). The extra anodic

peak at 2.35V is also caused by non-participating lithium. This causes a negative potential between lithium and silicon (~0.15 V), shifting the normal peak at 2.5 V down to 2.35 V.

Figure 3.3D shows the CV profile for the SSFC once it has reached equilibrium. The two cathodic peaks at 2.0 V and 2.3 V followed by an anodic peak at 2.5 V match the electrochemistry of sulfur half-cell, Figure 3.3A. This slight shift in peaks towards a higher potential represents complete activation of the lithium and further kinetic enhancement of the system.[35] The difference in current range between Figure 3.3C and Figure 3.3D is attributed to a change in the peak current, alluding to a higher capacity and reactivity.[37] This coincides with the increase in capacity as seen in Figure 3.5C.

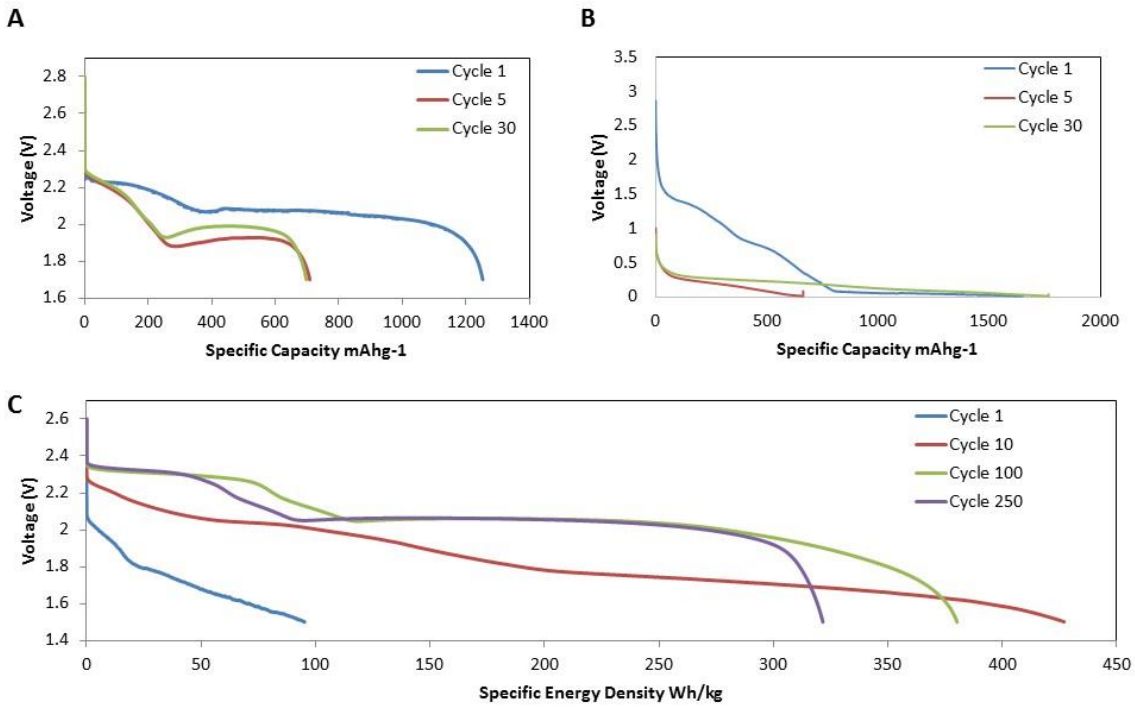

Figure 3.4 A) Galvanostatic voltage profiles for the sulfur electrode at C/10 for selected cycles. B) Galvanostatic voltage profiles for the silicon electrode at C/10 for selected cycles. C) Galvanostatic voltage profiles for the SSFC at C/10 for selected cycles.

The charge-discharge profiles for the SSFC, sulfur and silicon cells are shown in Figure 3.4. The potential of the sulfur half-cell during its first discharge in Figure 3.4A exhibits two long plateaus at 2.3 V and 2.1 V. The first long plateau at 2.3 V is associated with long chain polysulfide formation (Li_2S_X:x=8,6,4).[38] The second plateau at 2.1 V corresponds to the formation of Li_2S_2 and Li_2S.[38,39] After the first cycle, the plateau at 2.1 V shifts to 1.9 V due to the enhanced kinetics, which concurs with the CV profile in Figure 3.3A. The potential of the silicon half-cell during its first discharge in Figure 3.4B

exhibits a long plateau starting at 1.4 V. This corresponds to the formation of the solid electrolyte interphase.[24,40] The voltage plateau at 1.4 V disappears after the first cycle, and is replaced with a plateau at 0.2 V. This is in accordance with the cathodic peak seen in Figure 3.3B. The CV and discharge profiles for the sulfur and silicon half-cells are also consistent with data reported in literature.[3,29]

Figure 3.4C shows the discharge profile for the SSFC. The first cycle has plateaus at 2 V and 1.8 V which concur with Figure 3.3C. At cycle 2, an excess plateau at 1.8 V results from the aforementioned equilibrium potential between sulfur, silicon, and non-participating lithium. This speculation is further proven by the change of the 1.8V plateau, which becomes shorter as the test progresses, indicating less non-participating lithium. The voltage difference between the 10th and 100th cycles results from the cell conditioning and stabilizing by incorporating additional lithium over time. Once all the available lithium participates in the battery system, as shown in cycle 100 and 250, the voltage profile of the SSFC is in accordance with the sulfur half-cell. This proves that a stabilized SSFC act similar to a conventional full cell where cathode dominates the electrochemistry.[30,31]

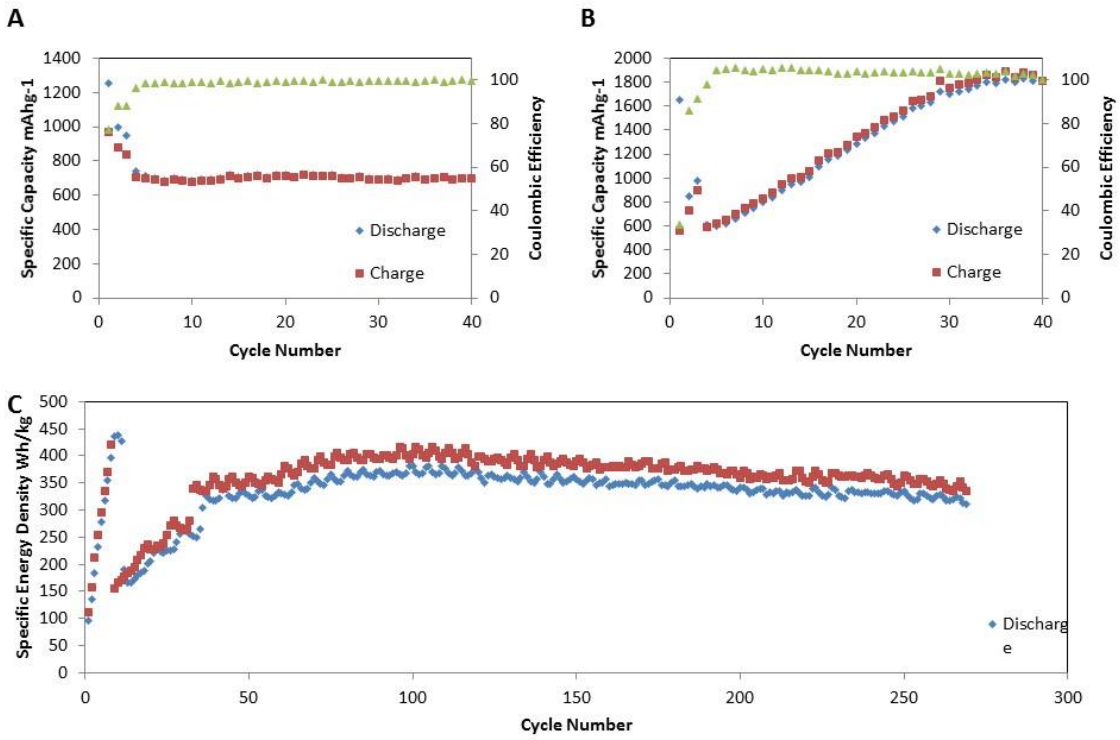

Figure 3.5 A) Galvanostic cycling of the sulfur electrode at C/10 for 40 cycles. B) Galvanostic cycling of the silicon electrode at C/10 for 40 cycles.) Deep Galvanostic cycling of the SSFC at C/10 for more than 250 cycles.

Galvanostatic cycling of the sulfur and the silicon half-cell was carried out at a potential window of 1.7–2.8 V and 0.01-1 V respectively. In Figure 3.5, the capacity for the batteries was measured at a rate of C/10 after being conditioned at C/50 for 3 cycles. The sudden decrease in performance at cycle 4 for both of the half cells is due to the rate change from C/50 to C/10. In Figure 3.5A, the sulfur half-cell has an initial capacity of 1254 mAh/g and maintains a capacity of 700 mAh/g for 40 cycles with a coulombic efficiency greater than 99%. The decrease in capacity is attributed to SEI formation,

polysulfide shuttling, as well as mechanical degradation of the electrode. In Figure 3.5B, the silicon half-cell has an initial capacity of 600 mAh/g and stabilizes at 1800 mAh/g within 40 cycles with a coulombic efficiency greater than 99%. The increase in capacity is attributed to the calendared electrode limiting the expansion of lithiated silicon and electrolyte penetration.[41] This coincides with Figure 3.3B, wherein the overall CV curve of the silicon half-cell increases in intensity over time, alluding to a higher capacity.[37]

Figure 3.5C shows galvanostatic cycling for the SSFC. The energy density of the SSFC, which is calculated based on the total anode and cathode weight (see supplementary information for details), is recorded for 250 cycles. The wave like fluctuations in capacity results from temperature changes occurring inside the testing room. The initial energy density of the SSFC is 100 Wh/kg at C/50 then increases to 414 Wh/kg over 10 cycles. The sudden drop in capacity at cycle 11 is due to the current rate change from C/50 to C/10. The increase in energy density is attributed to the continuous integration of non-participating lithium, shown in Figure 3.5C; this hypothesis is confirmed by Figures 3.3, 3.4, and 3.7. The SSFC has an energy density of 350 Wh/kg for over 250 cycles and a coulombic efficiency of approximately 95%. The fluctuation in coulombic efficiency from cycle 1 to 150 is due to the process of lithium integration, which creates a unique chemical reaction to the SSFC. When charging a conventional full-cell, lithium ions from the cathode travels to the anode while electrons travels through the outer circuit from cathode to anode as well, as a result, the anode materials are lithiated. Li-ions and the electrons are then returned to the cathode during discharge. In the SSFC, lithium starts on the anode side, thus discharge happens during the first

cycle. We propose that during discharge, lithium ions from the lithium chip travel to the cathode through electrolyte, while the electrons from the lithium chip travels through its contact point with the current collector and joins the electrochemistry process. However, in later cycles, lithium that is not directly in contact with the current collector can only join the system by either transferring electrons through the relatively insulating silicon slurry or by lithiating the silicon slurry during charge. This additional lithiation increases the charge capacity, which in turns decreases the coulombic efficiency. Hence, the coulombic efficiency of cycles 1 to 150 are low and unstable despite the cathode operates with a stable coulombic efficiency of 99%, shown in Figure 3.5A. After 150 cycles all required lithium is incorporated into the SSFC system and is actively participating in the redox reaction, however, excess lithium remains. During charge, lithium ions from the cathode plate onto the excess lithium chip while in parallel, lithium ions from the chip react with the silicon anode. As a result, the coulombic efficiency after 150 cycles have improved but are still in the range of 95% instead of being similar to the sulfur half-cell.

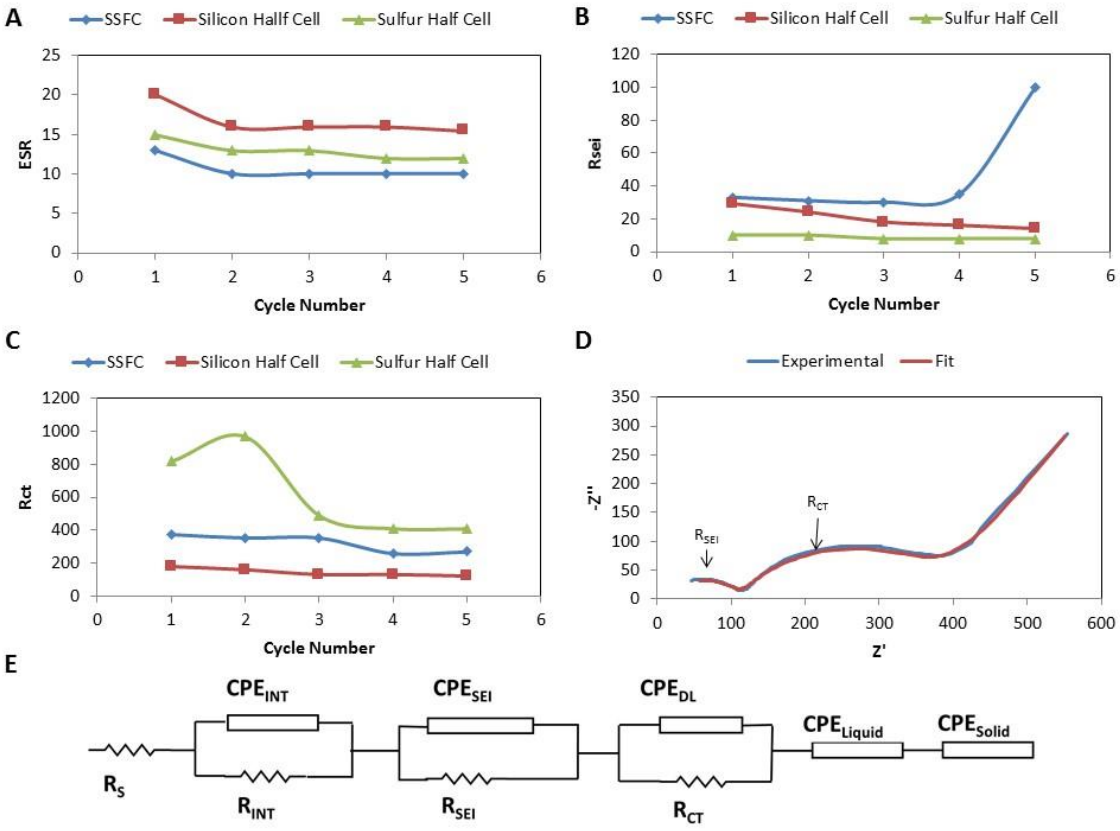

Figure 3.6 Impedance parameters during initial cycles for SSFC, silicon half-cell, and sulfur half-cell. A) ESR. B) R_{CT}. C) R_{SEI}. D) Experimental data SSFC cycle. 5 E) EEC used to obtain parameters.

Electrochemical impedance spectroscopy, shown in Figure 3.6, is a non-destructive method allowing us to investigate the integrity of electrode-electrolyte interface, passivation layers, electronic conductivity of electrode material, diffusion of lithium within electrode, and diffusion of lithium ions in electrolyte near electrode surface. Potentiostatic EIS is utilized to characterize the cells' complex impedance by measuring the current response to a small sinusoidal voltage signal. Impedance is

obtained for a selected number of frequency points between the bounds of 10 kHz and 10 mHz.

Figure 3.6E shows the electrical equivalent circuit used to model the impedance of lithium-ion cells at a fully charged state. A fit between the impedance response of the circuit and that of the cell is obtained by tuning the circuit parameter values. The constant phase elements (CPE) present in the circuit are capacitances that are spatially non-uniform. Equation 1 gives the formula used to calculate the impedance of CPE. Here Q is analogue to capacitance, and n is an ideality factor that is constrained between 0 and 1, while an ideality factor of 1 is identical to an ideal capacitor.

$$Z_{CPE} = \frac{1}{Q(j\omega)^n}$$

(1)

In Figure 3.6E, the value of equivalent series resistance (ESR) represents electrolyte conductivity. R_{INT} quantizes electronic conductivity within electrode matrix, while CPE_{INT} is a measure of the non-ideal capacitance that arises due to this finite conductivity. CPE_{FILM} and R_{FILM} quantize non-ideal capacitance and resistance associated with the passivating layers. CPE_{DL} measures the nature of the Helmholtz double-layer formed about the electrode-electrolyte interface, while R_{CT} determines the exchange current density. R_{CT} is an indicator of how facile electron exchange kinetics are at the interface. CPE_{LIQUID} quantizes diffusion of lithium ions in electrolyte near electrode surface. This diffusion impedance originates from the concentration gradient of lithium

ions existing between the diffuse layer of charge and bulk electrolyte. CPE_{SOLID} represents solid state diffusion of lithium atoms within the electrode material after lithiation and before delithiation.

Figure 3.6A shows the evolution of ESR during initial cycling in the SSFC and the sulfur/silicon half-cells. ESR in all three cells show a stabilizing trend, which provides evidence of electrochemical durability. It is observed that the two half-cells show a larger ESR than the SSFC. A previous study has shown that electrolyte decomposition is worse in half-cells due to the presence of lithium-metal counter electrodes.[42] Figure 3.6C shows the change in R_{CT} during the initial cycles in the same cells. It provides evidence for sulfur having slower kinetics than silicon. All three cells show a stabilizing trend over the initial cycles.

Figure 3.6B shows how R_{SEI} changes for the three cells within the same cycling window. Here we observe that the SSFC has the highest resistance value when compared to silicon and sulfur half-cells. We propose that the method we utilized to lithiate the full-cell assembly contributed to this observation. Lithium metal placed within the SSFC formed its own SEI during the initial cycling while the lithium content was slowly integrated into the anode. While the chip lost its lithium content to silicon anode, the SEI layer formed on top of it remained. Additionally, another SEI layer formed on the silicon anode as it participated in active lithiation/delithiation reactions. Thus, SSFC exhibits SEI impedance that originate from the silicon anode, from conductive carbon added in sulfur cathode, and from the lithium metal itself used to lithiate the full-cell. We also observe a spike in R_{SEI} at the end of the 5th cycle. We hypothesize that this spike occurs due to the

majority of SEI formation taking place on the silicon anode. We also observed that sulfur half-cell showed the lowest R_{SEI} value among the three cells. This is so because sulfur does not natively form any permanent passivation film similar to SEI layers observed in silicon or carbon electrodes. SEI impedance observed in our sulfur electrodes originate from the carbon additive added to the electrode matrix as conductive agent.

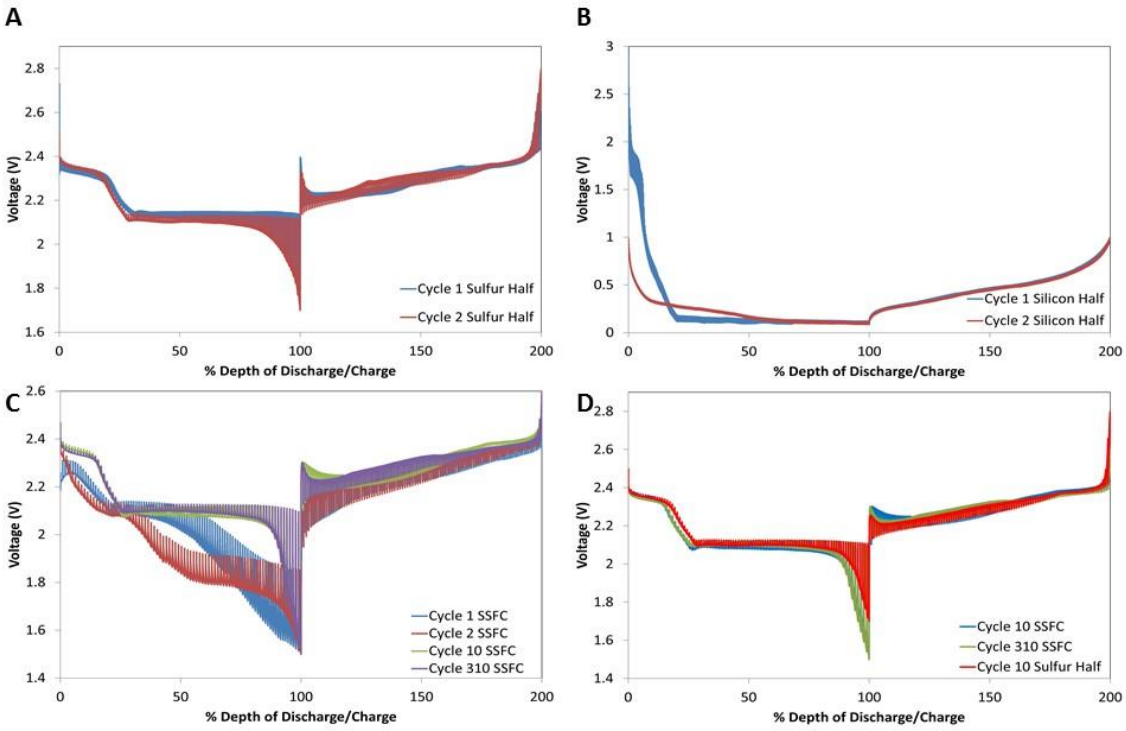

Figure 3.7 A) GITT analysis on the sulfur electrode at C/50 with 10 minutes rest for cycles 1-2. B).GITT analysis on the silicon electrode at C/50 with 10 minutes rest for cycles 1-2. C) GITT analysis on the SSFC at C/50 with 10 minutes rest for cycles 1, 2, 10, 310. D) GITT analysis comparing sulfur electrode at cycle 10 vs SSFC at cycles 10,310.

GITT, shown in Figure 3.7, was employed to investigate changes in lithium diffusivity within the individual battery systems.[43,44] The batteries were subjected to current pulse intervals with a rate of C/50 for 10 minutes, followed by 10 minute rests until complete discharge/charge. In Figure 3.7, the varying thickness of the voltage profiles represent varying lithium diffusivities in the system. Thinner voltage profiles indicate improved diffusivity while thicker voltage profiles represent the inverse.[45,46]

In Figure 3.7A, the profile for the sulfur half-cell displays a slight decrease in voltage plateaus from cycles 1 to 2. This occurrence is also observed in Figure 3.3A & 3.4A, and is attributed to the change in ionic and electric conductivity caused by the incremental SEI formation and polysulfide shuttling.[44] As seen in Figure 3.7B, the silicon half-cell experiences a voltage shift within the first two cycles; this is attributed to SEI formation, coinciding with Figure 3.4B. However, voltage profiles and diffusivity equilibrate by the second cycle, indicating that the silicon half-cell has faster kinetics than the sulfur half-cell as inferred by Figure 3.6C. Hence, it is determined that the kinetics of sulfur half-cell is the limiting factor for the diffusivity of the SSFC.

Figure 3.7C shows the GITT profile for the SSFC. Figure 3.7C depicts the voltage profiles of the SSFC resembling the sulfur half-cell, revealing plateaus at 2.3 V and 2.1 V after reaching equilibrium. However, the first cycle of the SSFC shows a discharge profile offset from the sulfur half-cell; this is attributed to limited lithium participation in the first cycle. The excess voltage plateau in cycle 2, at roughly starting at 50% depth of discharge, alludes to the Li incorporation issues associated with the architecture of the cell. The broad voltage fluctuation in cycles 1-2's GITT profile indicate a nonuniform

material utilization caused by part of the electrode not being lithiated with the limited participating lithium, supporting the aforementioned speculation. At cycle 10, the voltage profile of SSFC already resembles a sulfur half-cell. The observable change in diffusion in cycle 2 to 10 is a result of total lithium utilization allowable in the system. This change in the voltage profile comparing to normal cycling, figure 3.4C, is due to the pulsed discharge currents of GITT progressing the cell at a faster rate allowing complete lithium integration by cycle 10. Once reaching complete lithium utilization, the diffusivity of the system continue to improve from cycles 10 to 310. Thinner voltage profiles as well as a higher voltage plateau are observed in the subsequent cycles, which is a result of enhanced kinetics.

Figure 3.7D compares the diffusivity of SSFC to the sulfur half-cell, wherein we see a notable difference within the early cycles. At 80 - 100% depth of discharge, the observable difference in diffusivity from the half-cell to SSFC is caused by the charge transfer resistance of the silicon anode. Similarly, once the cell starts to charge, the notable difference in diffusivity profiles at 0-20% depth of charge is a result of charge transfer resistance in the cathode for the SSFC. Ultimately, Figure 3.7D depicts the SSFC voltage profile continues to coincide with that of the half-cell once it has developed a complete utilization of lithium.

3.4 Conclusion

Herein, we have presented a simple alternative to prelithiated sulfur-silicon full cell systems by allowing lithium access to the external circuit. In addition, this method

allows for the controlled loading of lithium to compensate for SEI formation and lithium degradation. As a new full cell configuration for next generation lithium ion batteries, the SSFC demonstrates an energy density of 350 Wh/kg over 250 cycles at C/10. Furthermore, this is the first time, to the best of our knowledge, a sulfur silicon full cell has been fully characterized using EIS, CV and GITT. The results presented will pave the way for new research into sulfur and silicon full cells.

3.5 References

1. Yin, Y. X., Xin, S., Guo, Y. G. & Wan, L. J. Lithium–sulfur batteries: electrochemistry, materials, and prospects. Angewandte Chemie International Edition 52, 13186-13200 (2013).

2. Choi, N.S., Chen, Z., Freunberger, S.A., Ji, X., Sun, Y.K., Amine, K., Yushin, G., Nazar, L.F., Cho, J. and Bruce, P.G. Challenges Facing Lithium Batteries and Electrical Double-Layer Capacitors. Angewandte Chemie International Edition 51, 9994-10024 (2012).

3. Zhao, X., Cheruvally, G., Kim, C., Cho, K.K., Ahn, H.J., Kim, K.W. and Ahn, J.H. Lithium/Sulfur Secondary Batteries: A Review. JOURNAL OF ELECTROCHEMICAL SCIENCE AND TECHNOLOGY 7, 97-114 (2016).

4. Scrosati, B. Recent advances in lithium ion battery materials. Electrochimica Acta 45, 2461-2466 (2000).

5. Tarascon, J.-M. & Armand, M. Issues and challenges facing rechargeable lithium batteries. Nature 414, 359-367 (2001).

6. Lu, L., Han, X., Li, J., Hua, J. & Ouyang, M. A review on the key issues for lithium-ion battery management in electric vehicles. Journal of power sources 226, 272-288 (2013).

7. Barré, A., Deguilhem, B., Grolleau, S., Gérard, M., Suard, F. and Riu, D. A review on lithium-ion battery ageing mechanisms and estimations for automotive applications. Journal of Power Sources 241, 680-689 (2013).

8. Park, H., Koh, H. S. & Siegel, D. J. First-Principles Study of Redox End Members in Lithium–Sulfur Batteries. The Journal of Physical Chemistry C 119, 4675-4683 (2015).

9. Wu, F., Lee, J.T., Nitta, N., Kim, H., Borodin, O. and Yushin, G. Lithium iodide as a promising electrolyte additive for lithium–sulfur batteries: mechanisms of performance enhancement. Advanced Materials 27, 101-108 (2015).

10. Zhang, S. S. Liquid electrolyte lithium/sulfur battery: fundamental chemistry, problems, and solutions. Journal of Power Sources 231, 153-162 (2013).

11. Manthiram, A., Fu, Y. & Su, Y.-S. Challenges and prospects of lithium–sulfur batteries. Accounts of chemical research 46, 1125-1134 (2012).

12. Canas, N.A., Hirose, K., Pascucci, B., Wagner, N., Friedrich, K.A. and Hiesgen, R. Investigations of lithium–sulfur batteries using electrochemical impedance spectroscopy. Electrochimica Acta 97, 42-51 (2013).

13. Pang, Q., Liang, X., Kwok, C. Y. & Nazar, L. F. Advances in lithium–sulfur batteries based on multifunctional cathodes and electrolytes. Nature Energy 1, 16132 (2016).

14. Li, Z., Zhang, J. & Lou, X. W. D. Hollow Carbon Nanofibers Filled with MnO2 Nanosheets as Efficient Sulfur Hosts for Lithium–Sulfur Batteries. Angewandte Chemie International Edition 54, 12886-12890 (2015).

15. Shan, J., Liu, Y., Su, Y., Liu, P., Zhuang, X., Wu, D., Zhang, F. and Feng, X. Graphene-directed two-dimensional porous carbon frameworks for high-performance lithium–sulfur battery cathodes. Journal of Materials Chemistry A 4, 314-320 (2016).

16. Balach, J., Jaumann, T., Klose, M., Oswald, S., Eckert, J. and Giebeler, L. Functional Mesoporous Carbon-Coated Separator for Long–Life, High–Energy Lithium–Sulfur Batteries. Advanced Functional Materials 25, 5285-5291 (2015).

17. Zhang, L., Ji, L., Glans, P.A., Zhang, Y., Zhu, J. and Guo, J. Electronic structure and chemical bonding of a graphene oxide–sulfur nanocomposite for use in superior performance lithium–sulfur cells. Physical Chemistry Chemical Physics 14, 13670-13675 (2012).

18. Su, X., Wu, Q., Li, J., Xiao, X., Lott, A., Lu, W., Sheldon, B.W. and Wu, J. Silicon–based nanomaterials for lithium-ion batteries: a review. Advanced Energy Materials 4 (2014).

19. Zhang, W.-J. A review of the electrochemical performance of alloy anodes for lithium-ion batteries. Journal of Power Sources 196, 13-24 (2011).

20. McDowell, M. T., Lee, S. W., Nix, W. D. & Cui, Y. 25th Anniversary Article: Understanding the Lithiation of Silicon and Other Alloying Anodes for Lithium-Ion Batteries. Advanced Materials 25, 4966-4985 (2013).

21. Liang, B., Liu, Y. & Xu, Y. Silicon-based materials as high capacity anodes for next generation lithium ion batteries. Journal of Power sources 267, 469-490 (2014).

22. Chan, C. K., Ruffo, R., Hong, S. S. & Cui, Y. Surface chemistry and morphology of the solid electrolyte interphase on silicon nanowire lithium-ion battery anodes. Journal of Power Sources 189, 1132-1140 (2009).

23. Wu, H., Zheng, G., Liu, N., Carney, T.J., Yang, Y. and Cui, Y. Engineering empty space between Si nanoparticles for lithium-ion battery anodes. Nano letters 12, 904-909 (2012).

24. Favors, Z., Wang, W., Bay, H.H., George, A., Ozkan, M. and Ozkan, C.S. Stable Cycling of SiO2 Nanotubes as High-Performance Anodes for Lithium-Ion Batteries. Scientific reports 4 (2014).

25. Teki, R., Datta, M.K., Krishnan, R., Parker, T.C., Lu, T.M., Kumta, P.N. and Koratkar, N. Nanostructured silicon anodes for lithium ion rechargeable batteries. Small 5, 2236-2242 (2009).

26. Li, X., Gu, M., Hu, S., Kennard, R., Yan, P., Chen, X., Wang, C., Sailor, M.J., Zhang, J.G. and Liu, J. Mesoporous silicon sponge as an anti-pulverization structure for high-performance lithium-ion battery anodes. Nature communications 5 (2014).

27. He, Y., Yu, X., Wang, Y., Li, H. & Huang, X. Alumina-Coated Patterned Amorphous Silicon as the Anode for a Lithium-Ion Battery with High Coulombic Efficiency. Advanced Materials 23, 4938-4941 (2011).

28. Kim, H., Han, B., Choo, J. & Cho, J. Three-dimensional porous silicon particles for use in high-performance lithium secondary batteries. Angewandte Chemie 120, 10305-10308 (2008).

29. Li, C., Liu, C., Wang, W., Mutlu, Z., Bell, J., Ahmed, K., Ye, R., Ozkan, M. and Ozkan, C.S. Silicon Derived from Glass Bottles as Anode Materials for Lithium Ion Full Cell Batteries. Scientific Reports 7, 917 (2017).

30. Yang, Y., McDowell, M.T., Jackson, A., Cha, J.J., Hong, S.S. and Cui, Y. New nanostructured Li2S/silicon rechargeable battery with high specific energy. Nano letters 10, 1486-1491 (2010).

31. Hassoun, J., Kim, J., Lee, D.J., Jung, H.G., Lee, S.M., Sun, Y.K. and Scrosati, B. A contribution to the progress of high energy batteries: A metal-free, lithium-ion, silicon–sulfur battery. Journal of Power Sources 202, 308-313 (2012).

32. Liu, N., Hu, L., McDowell, M. T., Jackson, A. & Cui, Y. Prelithiated silicon nanowires as an anode for lithium ion batteries. Acs Nano 5, 6487-6493 (2011).

33. Zhang, S. S. Role of LiNO3 in rechargeable lithium/sulfur battery. Electrochimica Acta 70, 344-348 (2012).

34. Cai, K., Song, M.-K., Cairns, E. J. & Zhang, Y. Nanostructured Li2S–C composites as cathode material for high-energy lithium/sulfur batteries. Nano letters 12, 6474-6479 (2012).

35. Ji, L., Rao, M., Aloni, S., Wang, L., Cairns, E.J. and Zhang, Y. Porous carbon nanofiber–sulfur composite electrodes for lithium/sulfur cells. Energy & Environmental Science 4, 5053-5059 (2011).

36. Favors, Z., Wang, W., Bay, H.H., Mutlu, Z., Ahmed, K., Liu, C., Ozkan, M. and Ozkan, C.S. Scalable Synthesis of Nano-Silicon from Beach Sand for Long Cycle Life Li-ion Batteries. Scientific reports 4 (2014).

37. Bell, J., Ye, R., Ahmed, K., Liu, C., Ozkan, M. and Ozkan, C.S. Free-standing Ni–NiO nanofiber cloth anode for high capacity and high rate Li-ion batteries. Nano Energy 18, 47-56 (2015).

38. Chen, J.J., Yuan, R.M., Feng, J.M., Zhang, Q., Huang, J.X., Fu, G., Zheng, M.S., Ren, B. and Dong, Q.F. Conductive Lewis Base Matrix to Recover the Missing Link of Li2S8 during the Sulfur Redox Cycle in Li–S Battery. Chemistry of Materials 27, 2048-2055 (2015).

39. Ji, X., Lee, K. T. & Nazar, L. F. A highly ordered nanostructured carbon–sulphur cathode for lithium–sulphur batteries. Nature materials 8, 500-506 (2009).

40. Favors, Z., Bay, H.H., Mutlu, Z., Ahmed, K., Ionescu, R., Ye, R., Ozkan, M. and Ozkan, C.S. Towards Scalable Binderless Electrode: Carbon Coated Silicon Nanofiber Paper via Mg Reduction of Electrospun SiO2 Nanofibers. Scientific reports 5, 8246 (2015).

41. Vlad, A., Reddy, A.L.M., Ajayan, A., Singh, N., Gohy, J.F., Melinte, S. and Ajayan, P.M. Roll up nanowire battery from silicon chips. Proceedings of the National Academy of Sciences 109, 15168-15173 (2012).

42. Delpuech, N., Dupre, N., Moreau, P., Bridel, J.S., Gaubicher, J., Lestriez, B. and Guyomard, D. Mechanism of Silicon Electrode Aging upon Cycling in Full Lithium–Ion Batteries. ChemSusChem (2016).

43. Gagneur, L., Driemeyer-Franco, A., Forgez, C. & Friedrich, G. Modeling of the diffusion phenomenon in a lithium-ion cell using frequency or time domain identification. Microelectronics Reliability 53, 784-796 (2013).

44. Busche, M.R., Adelhelm, P., Sommer, H., Schneider, H., Leitner, K. and Janek, J. Systematical electrochemical study on the parasitic shuttle-effect in lithium-

sulfur-cells at different temperatures and different rates. Journal of Power Sources 259, 289-299 (2014).

45. Park, J.W., Yamauchi, K., Takashima, E., Tachikawa, N., Ueno, K., Dokko, K. and Watanabe, M. Solvent effect of room temperature ionic liquids on electrochemical reactions in lithium–sulfur batteries. The Journal of Physical Chemistry C 117, 4431-4440 (2013).

46. Park, M.S., Yu, J.S., Kim, K.J., Jeong, G., Kim, J.H., Yim, T., Jo, Y.N., Hwang, U., Kang, S., Woo, T. and Kim, H. Porous carbon spheres as a functional conducting framework for use in lithium–sulfur batteries. RSC Advances 3, 11774-11781 (2013).

Chapter 4: Advanced Sulfur-Silicon Full Cell Architecture for Lithium Ion Batteries

4.1 Introduction

With demand for fossil fuels in decline while clean energy becoming more cost efficient, automotive companies are adopting electric vehicles (EV) for future transportation needs. However, current lithium ion battery (LiB) technologies are not capable of the performance required for EVs to be economically competitive with internal combustion engines. Conventional EV battery packs utilize lithium nickel manganese cobalt oxide (NMC) or lithium nickel cobalt aluminum oxide (NCA) cathodes capable of up to 300 highway miles due to a limited cathode capacity of 170 mAh/g. In order to facilitate further implementation of EVs, battery technologies capable of yielding longer driving ranges at lower prices need to be explored. One of the primary materials under consideration for next generation of LiBs is sulfur. Sulfur is a high capacity, energy dense, and abundant cathode material with a theoretical capacity of 1675 mAh/g and energy density of 2600 Wh/kg. However, lithium-sulfur (Li-S)s' electrochemistry presents several challenges that inhibit it from being commercialized.[1]

Li-S batteries face three major challenges: detrimental volumetric changes, poor electrical conductivity, and polysulfide shuttling.[2] Volumetric changes result from the density difference between sulfur and lithium sulfide.[3] An 80% volume change mechanically expands and contracts the electrode, degrading its structure and conductive network with each cycle. Sulfur's poor electrical conductivity requires a large amount of

carbon additive to achieve practical current rates greater than C/10 or 1.675 mAh/g.[4] However, excess additives decrease an electrode's sulfur content and creates deadweight in the electrode. This limits the cell's potential energy density, making it impractical for industry. Polysulfide shuttling in Li-S results from the long chain polysulfides (Li_2S_8 - Li_2S_4) being highly soluble in ether electrolytes, which are commonly used in Li-S batteries due to their preferred high ionic conductivity.[5] Once (Li_2S_8 - Li_2S_4) dissolves in the ether-based electrolyte, polysulfides shuttle from the sulfur electrode across the separator collecting on the counter electrode (lithium foil). These polysulfides form an insulating layer during delithiation, reducing ionic conductivity while causing capacity loss from dead sulfur.[6]

Various methods have been demonstrated to alleviate these aforementioned issues in sulfur's electrochemistry, each having varying degrees of improvement on the cell's performance. For example, to prevent mechanical pummeling in sulfur electrodes, researchers have proposed using the structures engineered with void spaces.[7] The engineered void spaces have extra room to accommodate expansion of sulfur but reduces the overall volumetric energy density of the cell. To tackle the issues of poor electrical conductivity, a combination of carbon nanotubes (CNTs), graphene, reduced graphene oxide (rGO), and other assorted highly conductive carbons in varying amounts have been utilized.[8-11] The conductive carbons help mitigate conductivity issues but at the expense of adding weight to the battery and increasing cost. To suppress polysulfide shuttling, several groups have employed various thin films or core shell structures such as graphene paper and pomegranate like carbon structures.[12,13] These structures trap polysulfides

within the cathode, increasing performance; however, the methods utilized to achieve this are impractical for commercialization.[14] Beyond issues in Li-S material electrochemistry, issues exist in the Li-S battery electrochemistry.

Common issues in Li-S battery electrochemistry resulting from cycling are electrolyte degradation, poor solid electrolyte interphase (SEI) formation, and gas evolution. All of these are common issues found in all LiB systems.[15,16] Among these issues, it is a consensus amongst researchers that SEI formation plays a key role in mitigating the negative behavior of the Li-S electrodes. The most common method for alleviating SEI formation issues is using supplemental additives, such as phosphorous pentasulfide, lithium nitrate, polysulfides, and lithium iodide.[17-20] Additive use focusing on robust SEI formation falls under three categories: reduction type, reaction type, and morphology modifier. However, additive use in Li-S tends to have adverse effects on energy density, internal resistance, and cycling stability while additive-free approaches to robust SEI formation have not garnered enough attention.[21,22]

Herein, we develop an additive free conditioning technique towards robust SEI formation that targets specific voltage plateaus Li-S batteries. Current practice in Li-S batteries is to slowly discharge/charge (C/20 - C/100) for one to three cycles before increasing to higher current rates.[23-27] However, conditioning practices are seldom understood, yet it has the potential to increase cell performance at little cost regardless of electrode design. We present three different methods for conditioning a Li-S cell tested by models inspired by city and highway driving conditions. Performance and health effects of the three conditioning methods on the cells are investigated using galvanostatic

intermittent titration technique (GITT), cyclic voltammetry (CV), galvanostatic cycling with potential limitation (GCPL), and potentiostatic electrochemical impedance spectroscopy (PEIS). All batteries are cycled under the same city and highway models to ensure comparable results. Currents are calculated based on information gathered from EVs driving rates. Below we show a novel additive-free approach to robust SEI formation for enhanced cycling performance characterized via custom testing models.

4.2 Experimental Details

4.2.1 Material synthesis

The battery used for the EV testing consists of a sulfur electrode countered by a lithium metal anode. The sulfur electrode was made with 20 wt% poly(acrylic acid) (PAA, 1800 g/mol, Sigma-Aldrich), and 80 wt% acetylene black sulfur composite (ABS) that was made by dissolving 200 mg of sulfur (S, 99.998% trace metals basis, Sigma-Aldrich) in 20 ml of dimethyl sulfoxide (DMSO, Fisher Chemical) at 90 C, heated by a heating jacket (Brisk Heat). 129 mg of acetylene black (Alfa Aesar, 50% compressed) was then added to the solution. The solution was stirred for 3 hours before the heating jacket was removed, and the solution was allowed to cool while stirring. The resulting ABS composite was then washed by anhydrous ethanol (Decon Labs, Inc.) several times to ensure the removal of DMSO and dried at 60 C for 24 hours. To make the sulfur electrode, 20 wt% PAA (450,000 MW) and 80wt% ABS was mixed with 1-methyl-2-pyrrolidinone (NMP, Sigma-Aldrich) and then casted on a large piece of aluminum foil (Alfa Aesar, 0.025 mm thickness, 99.45% purity) by a doctor blade (MTI Automatic

Thick Film Coater, BYK Doctor Blade). The casted electrode sheet was then dried in a convection oven (Cole-Parmer, Stable Temp) at 60 C for 24 hours. The electrodes were calendered with 0.04 mm gap using a calendering machine (IRM) before being constructed into a coin cell.

4.2.2 Electrochemical characterization

To make the sulfur half cell, a lithium foil electrode (16 mm in diameter) was first put inside a negative cap (MTI type 2032 coin cell case). Next, separators (Celgard 25 μm 3501) of various sizes were placed on top to prevent any possibility of shorting. Sulfur electrode (16 mm in diameter) was then placed on top followed by two spacers, a spring, and the positive cap while electrolyte was added in between (1:1 DOL:DME, 1wt% $LiNO_3$, 1M LiTFSI). The battery was then sealed using a battery crimper (MTI, MSK-160D). All cell assembly was done inside an Ar filled glovebox (H_2O < 0.5 ppm, O_2 < 0.2 ppm, Vacuum Atmosphere Co.). The battery was then tested under room temperature with a Bio Logic (BCS 810 Testing Module) using different testing methods, including GCPL, CV, PEIS and GITT in voltage window ranging from 1.7 V to 2.8 V.

4.3 Results and discussion

Various battery testing methods were used to evaluate cells pre/during/post simulated driving. The sulfur electrodes were made using an ABS composite with PAA as detailed in the methods section. The Li-S cells were then assembled into coin cells with lithium foil acting as the counter electrode. The sulfur loading for each battery is 2.5

mg/cm^2. The cells were then conditioned using three different methods: Method 1 applies a current rate of C/50 (0.175 mA) during discharge and charge for 3 cycles. This is the common average of conditioning methods reported by researchers and thus it was used as the datum in this study. Method 2 applies current pulses at 10 minute intervals at C/50 for 3 cycles. The rest between current pulses allows for voltage equalization, which will prolong the discharge process and maximize material reduction in the electrode. Lastly, Method 3 applies a rate of C/50 during discharge from 2.8 V to 2.1 V and a rate of C/100 (0.0875 mA) from 2.1 V to 1.7 V. This method avoids excess polysulfide shuttling in the voltage plateau associated with the formation of long chain polysulfides, while targeting the lower voltage plateau, at a slower rate, associated solid formation on the carbon matrix, 2.1 V. All methods charge batteries at a rate of C/50; each conditioning procedure is repeated for three cycles. Figure 4.4c-f, the proposed schematic for datum and plateau targeted conditionings effect on SEI formation along with the resulting effects on the battery system. A unconditioned control battery was tested in conjunction.

The cells then underwent two different testing models, one based on real world driving conditions found in the city (city model) and the other based on real world driving conditions found on the highway (highway model). Each model simulates a driving distance of 36.5 miles, the average distance driven by a person each day. At the end of each simulated day cells were fully charged, simulating users charging EVs overnight, and PEIS was taken. This driving/charging cycle was repeated 7 times (week) before a cycle of GITT. GITT was used to examine lithium diffusivity within the cell, giving a detailed picture of changes to the electrodes conductive network. Ten full

discharge/charge cycles were then applied to the cell to simulate aging. Post aging, CV was instituted to check the health of electrochemical reactions. Lastly, the driving-charging-PEIS-GITT-aging-CV process was repeated four times while doing PEIS at points of interest.

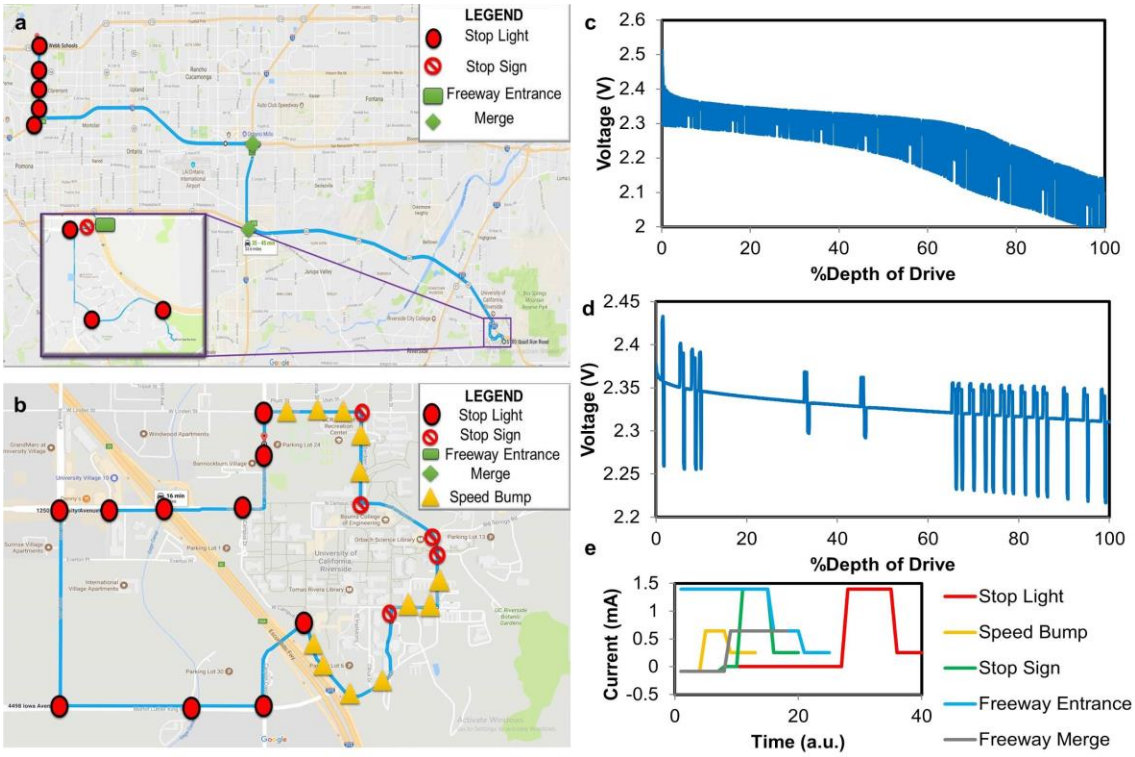

Figure 4.1 (a) Map of city driving route from google maps. (b) Map of highway driving route from google maps. (c) Voltage variation of Method 1 battery going through city cycling model (Riverside/Claremont, CA). (d) Voltage variation of Method 1 battery going through highway cycling model. (e) Current change of each simulated condition used in city and highway model.

The city model was designed to simulate different discharge/charge rates a EV battery was subjected to while driving in a city. Contrary to conventional constant current rated cycling used in research, the city model consists of a series of different

discharge/charge rates reflecting different energy consumption needs in a EV. To simulate real world driving conditions, corresponding discharge/charge rates were estimated based on data released for the Tesla Model S. From Tesla's official website, the discharge rate of the 75D Model S is around C/5 at 60 mph.[28] Considering that the specific capacity of a Li-S cell is 6 times the specific capacity of current commercial cells, the base discharge rate used for the city and highway models was calculated as C/30. Based on the constant driving condition, light and hard acceleration were simulated using C/10 and C/5; C/100 was used to simulate energy recovery during braking. A driving route was designed based on Google maps, shown in Figure 4.1a, consisting of lights, stop signs, turns, freeway mergers, freeway entrances/exits and speed bumps. Figure 4.1e shows the detailed rate changes of the city model. In a similar fashion, a highway model was designed, Figure 4.1b. Comparatively, the highway model contains less current rate variation resulting in a reduced stress load for batteries tested on the highway model. As a result, city and highway cycled batteries give different performance characteristics. Current rates associated with different speeds can be found in table S1, while common driving variable test protocols can be found in table 1.

Figure 4.1c and 4.1d, voltage fluctuations of city and highway models, respectively, during a simulated driving day. According to Figure 4.1c, a fully charged battery experiencing severe current fluctuation from the city model will discharge to around 2 V. Crossing the 2.1 V threshold indicates that the battery has passed the higher kinetic region (Li_2S_8-Li_2S_3) entering the lower kinetic region (Li_2S_2-Li_2S).[29] Figure 4.1d, batteries experiencing reduced current fluctuation from the highway model will remain in

the higher kinetic region (Li_2S_8-Li_2S_3). The difference in end voltages is an indicator of stresses placed on the battery, although both simulate the same driving distance. Batteries cycled by the city model experienced increased stresses than those cycled by the highway model.

Table 4.1 Current rate used to simulate driving interactions

City & Highway Model		
Driving Interaction	**Condition**	**Current**
Stop Sign	Brake, Stop, Hard Acceleration, Constant Driving	C/100, 0, C/5, C/30
Speed Bump	Brake, Light Acceleration, Constant Driving	C/100, C/10, C/30
Stop Light	Brake, Rest, Hard Acceleration, Constant Driving	C/100, 0, C/5, C/30
Freeway Entrance	Hard Acceleration, Light Acceleration, Constant Driving	C/5, C/10, C/30
Freeway Merge	Brake, Light Acceleration, Constant Driving	C/100, C/10, C/30

PEIS is a non-destructive method that characterizes the integrity of the electrode-electrolyte interface, passivation layers, electronic conductivity of electrode material, diffusion of lithium within electrode, and diffusion of lithium-ions in electrolyte near electrode surface.[30] Complex impedance was measured for a selected number of frequency points between the bounds of 10 kHz and 10 mHz. Figure 4.3e shows the electrical equivalent circuit used to model the impedance of Li-S cells at a fully charged state. Additionally, raw experimental data along with the curve fitted experimental data is depicted in Figure 4.2e and 4.2f. All batteries for each testing model were investigated with PEIS post day of driving and post GITT, aging, and CV.

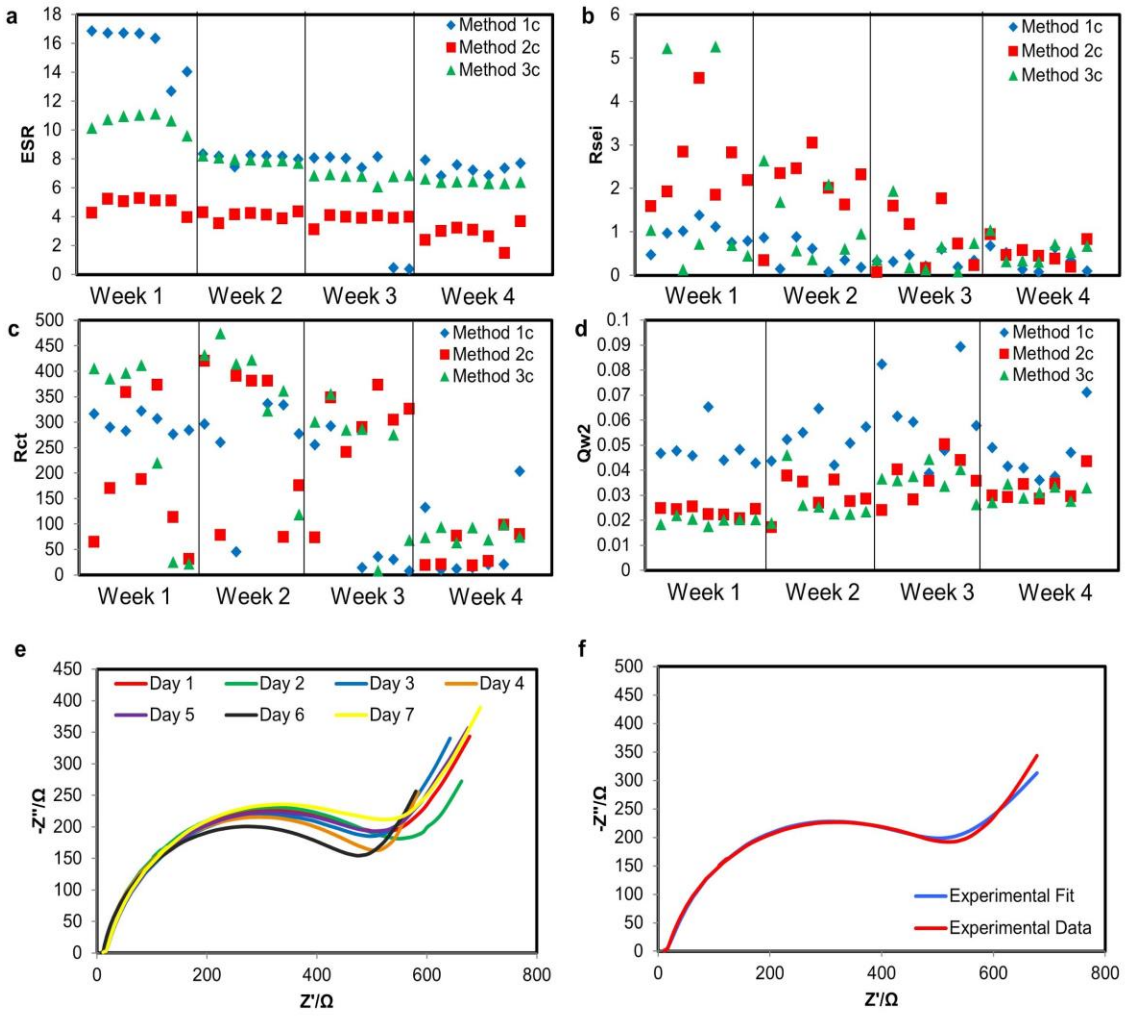

Figure 4.2 Impedance parameters of batteries tested by the city model after each driving days (a) ESR. (b) Rsei. (c) Rct. (d) Qw2. (e) Experimental PEIS curves for simulated week 1 of driving for Method 3. (f) Experimental data vs curve fitted data

Value of the equivalent series resistance (ESR) represents the total resistance contributed by solution resistance, charge transfer resistance, and contact resistance in the batteries.[30] Figure 4.2a shows the evolution of ESR for the city model. City ESR is highest for Method 1 battery and lowest for Method 2 battery. High ESR resistance for Method 1 battery can be attributed to the corrosion of the lithium metal anode. This

results from poor solid-electrolyte interphase (SEI) formation exhibited in Figure 4.2b by the low Rsei values. A previous study showed that once polysulfide concentration in the electrolyte passes a threshold (c > 0.5 M), polysulfides corrode the lithium metal, breakdown lithium SEI, form dendrites, and creates dead lithium[31]. This ultimately creates excess resistance in the lithium anode increasing ESR (Figure 4.2a). Contrarily, city ESR for Methods 2 and 3 batteries provide evidence of electrochemical durability, indicated by the stability in ESR from week 1 to 4. Electrochemical durability in a half cell is important but hard to achieve due to the presence of a lithium counter electrode, shown by Delpuech at el.[32] Method 1 battery shows a ESR drop from week 1, this concurs with drop in the Rct and an increase in Qw2 from week 1 to week 2 where Qw2 represents lithium capacitance in the electrolyte. Low ESR values for method 2 battery are attributed to changes in electrolyte ionic conductivity. Unlike method 1 battery, where it is believed the polysulfide electrolyte concentration passed a threshold, method 2 battery stayed in the beneficial range of polysulfide shuttling (0.1 M < c < 0.5 M). This prevents lithium corrosion while also enhancing ionic conductivity.[33] Therefore, method 2 battery which has more polysulfide shuttling, based of capacity differences, has the lowest ESR.[30] This difference in polysulfide shuttling is determined by SEI layer quality. Comparing to Method 2, Method 3's plateau targeted constant current rate allows formation of a robust SEI layer with minimal defects which greatly mitigates polysulfide shuttling. A secondary benefit of polysulfide mitigation is reducing parasitic effects on the lithium anode. Parasitic reactions cause the formation of an unstable SEI layer on the lithium anode, while stable SEI attributes greatly to the stability of the battery. A robust

SEI layer forming on both electrodes is supported by the stability in coulombic efficiency. The schematic for this proposed mechanism is depicted in Figure 4.4e and 4f.

Figure 4.2b shows Rsei changes for the city model. Rsei quantizes the resistance associated with the formation of the SEI layer, a higher Rsei indicates thicker SEI layers. Sulfur does not natively form any permanent passivation film similar to SEI layers observed in silicon or carbon electrodes.[34] We propose the SEI resistance observed in our sulfur electrodes mainly originate from the carbon additive but may also be affected by polysulfides and electrolyte composition. Shown in Figure 4.2b, it is observed that Method 2 battery has the highest resistance value compared to Methods 1 and 3 batteries. Method 2 battery's high Rsei results from the distinct characteristics of this conditioning method that utilized pulsed currents. We propose that the pulsed currents during the conditioning cycles cause volumetric expansion of sulfur to rupture the SEI layer prematurely formed during rest periods.[35] Each consecutive pulse repeats this detrimental process, causing an thick, nonhomogeneous SEI layer to form on the cathode, which results in inefficient lithium-ion conducting pathways.

The change in Rct for the city cycling is shown in Figure 4.2c. Rct is the charge transfer resistance at the electrode electrolyte interface which gives insights into the kinetics of the battery.[30] As shown in Figure 4.2c, all cells show a stabilizing trend in their kinetics during week 4. For weeks 1 to 3, all cells exhibit erratic behavior resulting from electrode degradation, mechanical or chemical, due to continued stresses placed on the cell by the city cycling model.

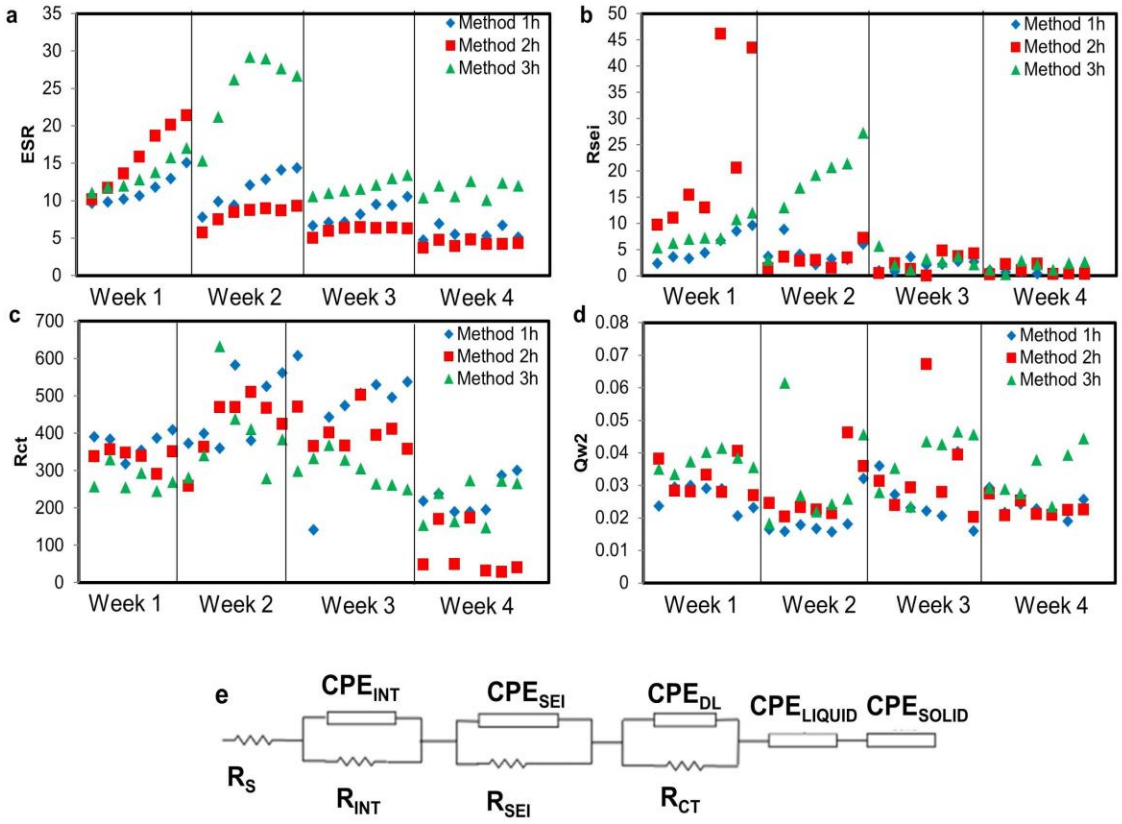

Figure 4.3 Impedance parameters of batteries tested by the highway model after each driving days (a) ESR. (b) Rsei. (c) Rct. (d) Qw2. (e) Electrical equivalent circuit used for PEIS.

The evolution of the ESR and Rsei for highway cycles is shown in Figure 4.3. ESR increases for all batteries week 1, but stabilizes by week 3. In contrast to Methods 1 and 2 batteries, ESR for Method 3 battery continue to increase during week 2. ESR is dominated by solution resistance, or electrolyte conductivity, but also considers changes in SEI resistance. This relationship is shown Figure 4.3b which the increase in ESR is attributed to the spike in Rsei week 2.

Rsei for all batteries increases during week 1 but stabilize by week 2 with the exception of Method 3 battery. In city cycling, it is observed that the SEI originates from the carbon additive but may also incorporate polysulfides into the measurement. For highway cycling, we propose that the structure of the delithiated polysulfides also affects the Rsei. The highway cycling model's discharge never reaches the second plateau (2.1 V), as shown in Figure 4.1d, indicating the sole formation of electrolyte soluble long chain polysulfides. During charge, each long chain polysulfides species (Li_2S_x, x=4-8) delithiates at the same rate into sulfur, the resulting sulfur particles gather on the conductive network and SEI layer. Sulfur gathering on the SEI layer can be mistaken as a contributing factor to Rsei. As sulfur becomes increasingly densified on the SEI layer with each successive cycle, Rsei increases proportionally, shown in Figure 4.3b. This phenomenon occurs in all batteries during week 1 but only exists for Method 3 battery in week 2. The increasing Rsei for Method 3 battery during week 2 results from it having a stronger SEI layer, mitigating polysulfide shuttling. It is speculated that the other two methods allow more sulfur loss located on the surface layers of the electrode to polysulfide shuttling, while Method 3 retained the majority of surface layer sulfur longer. Once the surface layer of sulfur is lost to polysulfide shuttling, Rsei stops increasing.

The change in Rct for the highway model is shown in Figure 4.3c. Week 1 to week 4 show a stabilizing trend for all batteries. Unlike the erratic behavior evidenced by Rct city cycling in Figure 4.2c, highway cycling does not experience this erratic behavior. We propose that the difference stems from the varying stresses placed on the batteries. Shown in Figure 4.1a and 4.1b, highway cycling only experiences 65 current rate changes

for total drive, compared to 270 current rate changes in city cycling. Hence the current rate changes in highway cycling do not cause sufficient stress to damage the electrode-electrolyte interface. As such, batteries subjected to all methods show stabilizing trends, with Method 3 battery experiencing the least resistance. Method 3 battery's low resistance results from a better electrode-electrolyte interface built during the conditioning cycles.

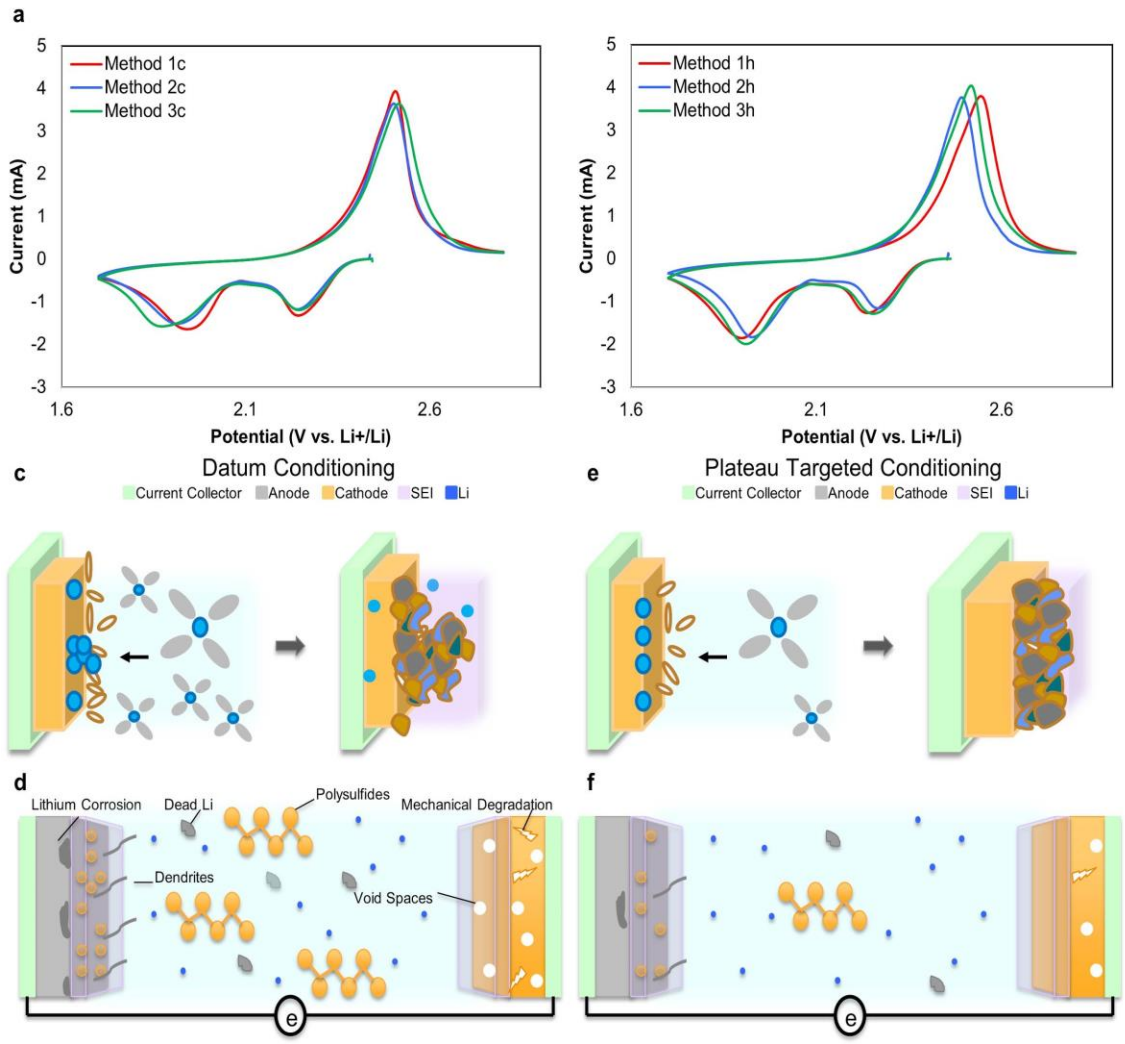

Figure 4.4 (a) CV of Method 1, 2, & 3 batteries tested by city model. (b) CV of Method 1, 2, & 3 batteries tested by highway model. (c) Proposed SEI formation for datum conditioning. (d) Proposed resulting effect of datum conditioning. (e) Proposed SEI formation for plateau targeted conditioning. (f) Proposed resulting effect of plateau targeted conditioning.

CV is an electrochemistry technique that measures current generated by the battery while cycling the battery potential at a given rate. When an electrode is cycled under CV, the reduction of electrode material causes current to increase forming a

cathodic peak. When the surface material has been reduced, lithium ions diffuse through the surface layer to continue the reduction process, thus causing the peak current to drop. As an adaption to the previous theory, a battery that has better kinetics will be able to reduce surface material faster, thus causing the cathodic peak to shift upward in potential. A battery that has greater quantity of active material to reduce will cause a greater peak intensity.[36]

CV for all batteries were carried out in a voltage window of 1.7 V and 2.8 V at a rate of 0.1 mV/s at each week end. Figure 4.4a and 4.4b show the CV profiles for batteries at week 4 end. The CV curves presented align with typical sulfur CV curves found in literature.[37] Sulfur's CV consists of two cathodic peaks at 2.1 V and 2.35 V, and one anodic peak at 2.35 V. The cathodic peak at 2.35 V corresponds to the formation of long chain polysulfides, while the peak at 2.1 V results from the formation of Li_2S. Slight variations in peak voltage between batteries result from different conditioning methods altering kinetics of the system. Peaks shifting towards a higher potential indicates a higher ionic conductivity stemming from increased polysulfides and SEI formation.[38] Variations in peak voltage is seen in both city and highway model batteries. Figure 4.4a, all city model batteries have the same anodic peak voltage of 2.25 V representing long chain polysulfide formation, while peaks representing Li_2S formation varies. Method 1 battery for the city model has the highest Li_2S peak voltage at 1.95 V, Method 2 and 3 batteries have a peak voltage of 1.9 V and 1.85 V respectively. Variance in peak voltage corresponding to Li_2S results from changes in ionic conductivity due to the differing concentration of polysulfides in the electrolyte.[33] As discussed in the previous section,

Method 3 battery is proposed to shuttle a reduced amount of polysulfides comparatively, resulting in the lowest peak voltage. In comparison, Method 1 with the highest quantity of polysulfides, results in the highest peak voltage. Method 1 and 3 batteries also have higher peak intensities than Method 2, indicating higher material reduction, this is further proven in Figure 4.7a.

Figure 4.4b shows the CV curves for the highway model batteries. Figure 4.4a and 4.4b, Method 1 battery for the highway model have lower cathodic and higher anodic peak voltages compared to Method 1 battery for the city model and the other two highway model batteries. The difference in peak voltages results from reduced cycling stress, minimizing polysulfide shuttling and mechanical degradation. The ionic conductivity boost, resulting from polysulfide shuttling in highway Method 1 battery does not compensate for the low ionic and electric conductivity resulting from poor SEI and conductive network. Method 2 and 3 batteries however, have well developed SEI and good mechanical stability. This result in Method 2 and 3 batteries having higher cathodic peak voltages and lower anodic peak voltages than Method 1 battery while having the same order (Method 2 battery peak voltage higher than Method 3 battery peak voltage) with city cycling CV following the same logic. Lastly, the peak intensity of Method 3 battery is the highest, followed by Method 1 and then Method 2 batteries, this is also in accordance with the trend shown in Figure 4.7b.

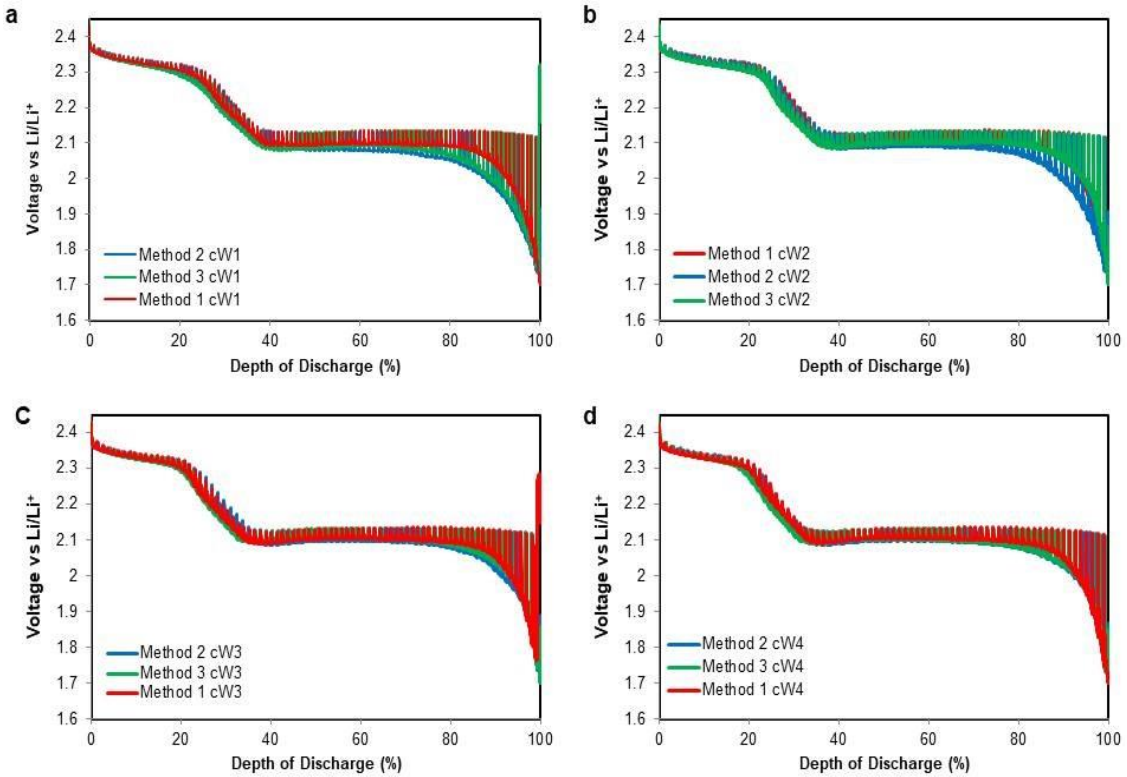

Figure 4.5 GITT for Methods 1,2, & 3 batteries after (a) week 1, (b) week 2, (c) week 3 and (d) week 4 of city model driving.

The driving models employed GITT once a week to measure the rate of lithium-ion diffusivity in the electrodes (Figure 4.5). GITT uses a series of current pulses, each followed by a relaxation period. Herein, electrodes were pulsed at C/50 for 10 minutes, immediately followed by 10 minutes rests. This interval was repeated until complete discharge/charge. Oscillations in the voltage profile represent changes between the pulsed voltages and steady state voltages.[39] Shorter oscillations throughout the voltage profile are ideal, indicating minimal voltage excitations during the relaxation period; this represents a homogenous material reduction and improved lithium diffusivity. However,

small oscillations may also be indicative of poor material access to the conductive network, referred to as material participation below.[40]

Figure 4.5a shows conditioning Method 1 yields the highest rate of lithium diffusivity amongst Methods 2 and 3 after 1 week of the city model. The high diffusivity rate is representative of a network with ease of Li ion transport, high ionic conductivity, and uniform material reduction. Ease of Li ion transport stems from a high concentration of polysulfide shuttling during the conditioning cycles. Consequently, vacancies are created in the electrode from polysulfide shuttling, decreasing material participation and creating better Li ion transport pathways. Additionally, shuttling increases polysulfide concentration in the electrolyte, producing a higher electrolyte ionic conductivity. Ultimately, these factors combined result in uniform material utilization. As a result, excitation of steady state voltage is minimized, and observed as shorter voltage oscillations in Figure 4.5a. The Method 1 battery has the smallest voltage oscillations in week 1 and remains as such due to poor material participation.

In contrast, Method 2 battery has the largest voltage oscillations, indicating slower overall rate of material reduction. We infer the overall slower material reduction is attributed to reduced polysulfide shuttling in addition to a larger active material to conductive network ratio. This large ratio results from the current pulses forcing additional active material to participate in the discharge reaction, furthering mechanical degradation. The low lithium diffusivity also results from the large SEI resistance (Figure 4.2b). A large SEI resistance decreases the overall diffusion rate of lithium-ions into the electrode, resulting in Method 2 battery as the least diffusing one. Method 3 battery's

improved diffusivity relative to Method 2 battery results from an effective conductive network and low SEI resistance. Method 3 battery's poor diffusivity relative to Method 1 battery however, is due to reduced polysulfide shuttling and increased sulfur utilization.

Ideally, ionic diffusivity in Li-S batteries should remain consistent throughout cycling. Consistency in diffusivity indicates steady active material utilization, minimal polysulfide shuttling, and electrode mechanical stability. However, in Figure 4.5b-d, voltage oscillations in each successive week decrease in width, indicating improved lithium diffusivity throughout the city model. The continuing changes in diffusivity results from active material loss, mechanical changes in the electrodes, decreased material participation, or changes in electrolyte polysulfide concentration. It is observed that the voltage oscillations for each battery in Week 4 of the city model are similar, resulting from the increase in ionic conductivity due to polysulfide shuttling. Once electrode degradation reaches the limit, all batteries reach similar conductivities and capacities (Figure 4.7). Differences in performance at the end of deep cycling is then determined by factors such as active material participation, SEI quality, mechanical stability, and conductive network quality in the electrodes. Ultimately, active material participation is the predominant variable contributing to ionic diffusivity at week 4 end in the city model.

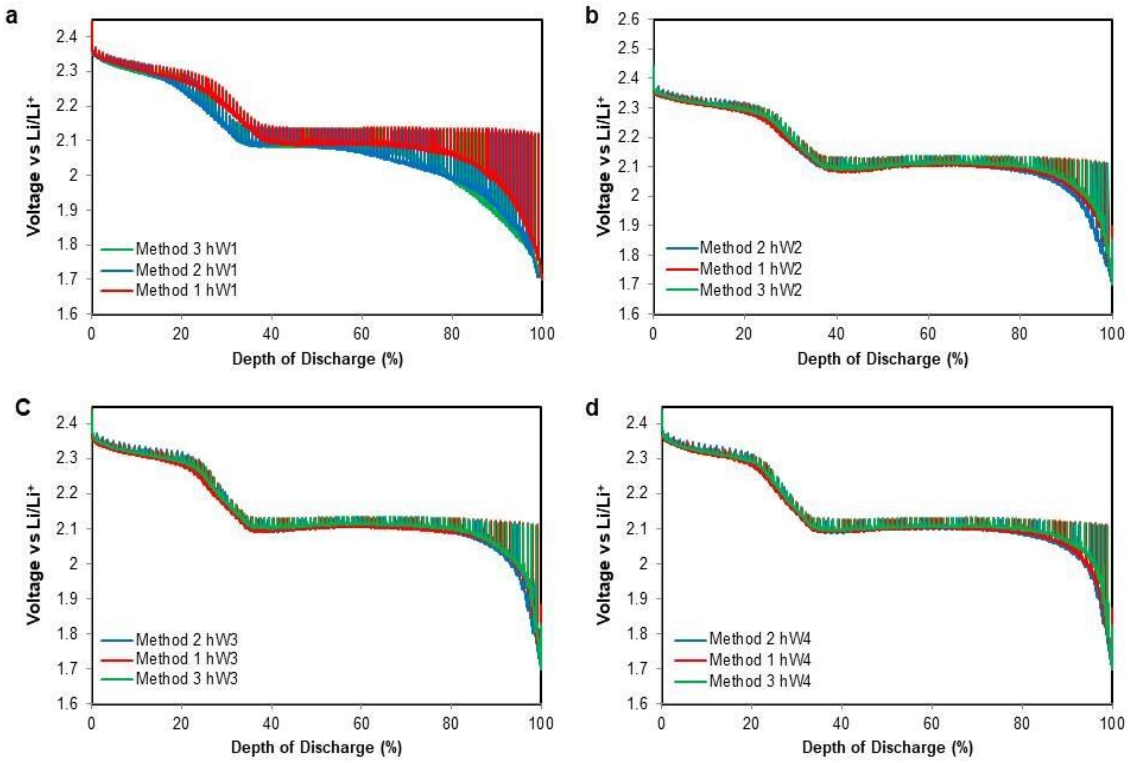

Figure 4.6 GITT for Methods 1,2, & 3 batteries after (a) week 1, (b) week 2, (c) week 3 and (d) week 4 of highway model driving.

GITT analysis of the highway model batteries differ starkly to the city model batteries, Figure 4.6. However, the trend is in accordance with the first two weeks of city model batteries. Highway model GITT profiles appear thinner than the city model profiles. This is due to the minimal amount of volume expansion created by less stressful highway model. As shown in Figure 4.1d, the batteries undergoing the highway model stayed in the first voltage plateau, indicating the sole formation of long chain polysulfides. Long chain polysulfides create up to 20% volumetric change compared to the 80% change in lithium sulfides formed during the second voltage plateau.[3] The small volume change causes the electrode to undergo minimal mechanical degradation resulting

in a better conductive network compared to the city model. Another explanation for the shorter voltage oscillations is stated in the PEIS section. As long chain polysulfides delithiate, delithiated polysulfides fall out of electrolyte and disperse evenly on the electrode's conductive network. As a result, the dispersed sulfur is homogeneously attached to the conductive network improving the electrical conductivity of the electrode. As such, method 2 battery does not experience much expansion, and is no longer the least diffusing, Figure 4.6a. In contrast, Method 1 experiences higher material participation, resulting in increased formation of long chain polysulfide within the first voltage plateau, relative to Method 2 and 3. This accounts for the first plateau of Method 1 to terminate at 40% depth of discharge versus Method 2 and 3 terminating at 35%. The diffusivity of the batteries after week 2 are in the order of polysulfide retention. Method 3 battery has the least polysulfide shuttling while having the worst diffusivity, Figure 4.6b. This is caused by a low concentration of polysulfides in the electrolyte. However, at the end of week 3 and 4, method 3 batteries' diffusivity increases and surpasses the other two batteries. This is because all batteries experience polysulfide saturation in the electrolyte over time and reach similar ionic conductivity, but method 3 battery's minimized mechanical degradation due to a robust SEI layer maintained the best electrical conductivity network. Contrary to city model, the conductive network is the predominant variable contributing to ionic diffusivity at week 4 in the highway model; low coulombic efficiency degradation for the highway model further supports this conclusion, Figure 4.7d.

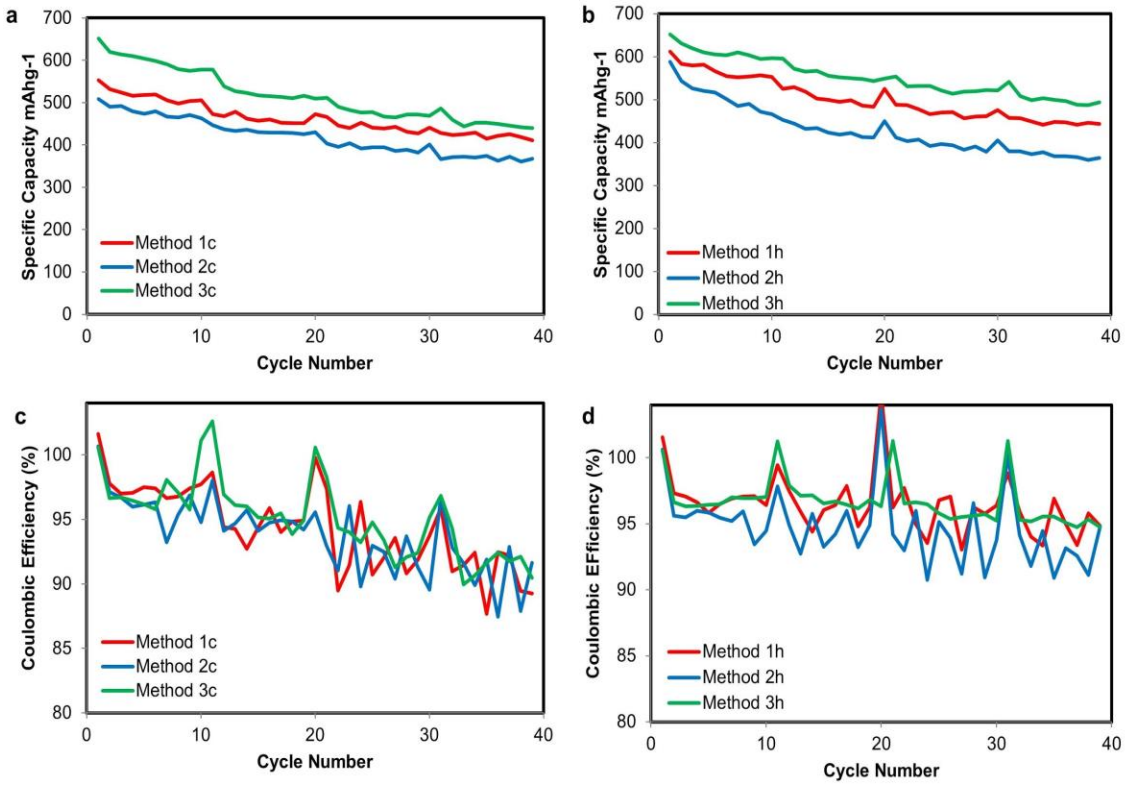

Figure 4.7 Galvanostatic cycling with limited potential for Method 1,2, & 3 batteries tested by city model (a) and highway model (b). Coulombic efficiency for Method 1, 2, & 3 batteries tested by city model (c) and highway model (d).

All batteries were discharged/charged for ten cycles post GITT to simulate aging. The corresponding specific capacity vs cycle number for each battery is shown in Figure 4.7a and 4.7b, respectively, for city and highway models. Wave like variation in capacity is caused by changes in room temperature during testing. All batteries show fluctuations in capacity due to temperature changes, it is observed that batteries undergoing condition method 3 fluctuate the least. This results from the stable and high quality SEI layer created during conditioning.[41] In both the city and highway model batteries, method 3 yields the highest capacity while method 2 yields the lowest. Since all batteries have the

same sulfur loading, a higher capacity is indicative of less active material loss during the previous testing routine and more material utilization during aging cycles. Active material loss can be a result of poor SEI layer causing polysulfide shuttling into the electrolyte and the counter electrode, or sulfur detaching from the conductive network during volume expansion/contraction.[30] Better material utilization can result from a better mechanical structure and SEI layer. The reliability of method 3 is observed by the similar starting capacity at city and highway aging cycle 1, city: 651 mAh/g, highway: 652 mAh/g. This aging cycle takes place after all batteries have been driven for 1 week followed by GITT. Method 1 and method 2 batteries however, show noticeable differences in the city and highway model capacities (City: 553 mAh/g and 509 mAh/g, highway: 612 mAh/g and 588 mAh/g). due to the more aggressive stresses of the city model. This indicates that method 3 yields superior capacity retention under stressed conditions.

Method 3 yields higher capacity batteries due to better SEI layer, which decreases further polysulfide shuttling. A robust SEI layer formed during conditioning prevents cracking of the SEI layer during high stress. This reduces material exposure to the electrolyte and prevents the generation of new and excess SEI. Furthermore, the robust SEI layer creates better mechanical stability and ionic pathways, which further stabilizes battery performance, resulting in 440 mAh/g city capacity and 494 mAh/g highway capacity after 4 weeks of testing. Method 2 yields the lowest capacities, 367 mAh/g for city and 364 mAh/g for highway at week 4, resulting from its increased volumetric expansion relative to the other methods. Volume expansion degrades lithium diffusivity

and rate capability of the battery. This is observed in Figure 4., where Method 2 battery yields larger voltage oscillation under the same current. GCPL capacity is measured by the amount of current battery can take at a specified unit of time before it reaches a set voltage, a large voltage fluctuation will result in a lower capacity. In conjunction with increased volumetric expansion, current pulses create excess SEI. Excess SEI consumes additional lithium salt, carbon additive, and lithium ions which can be attributed to the decreased capacity of Method 2 batteries. Method 1 batteries yields 411 mAh/g city capacity and 444 mAh/g highway capacity at week 4 end. This is due to a weaker SEI than Method 3 and less mechanical degradation than Method 2.

Due to the city model's increased stress relative to the highway model, rate of capacity degradation differs. Figure 4.7a shows the city model battery capacities converging toward an equilibrium point, 16.6% difference between method 2 and 3 batteries at the end, while Figure 4.7b shows the highway model battery capacities decreasing with similar rates, 26.3% difference between method 2 and 3 batteries at the end. The capacity convergence of the city model batteries is noticeable within the 40 aging cycles because of the high testing stress causing the battery to lose sulfur rapidly to polysulfide shuttling and mechanical degradation. Once the electrolyte reaches polysulfide saturation, the rate of capacity degradation slows down. As a result, all batteries will reach a similar final capacity, creating a converging capacity plot.

Figure 4.7c and 7d show the aging cycle coulombic efficiency (CE) for both city and highway models. Large spikes in CE up to 103% exist at the start of each aging cycle (1st, 11st, 21st, and the 31st cycle) due to GITT testing before aging cycles. GITT

disrupts the CE of the following cycle by overcharging the battery and activating sulfur that does not participate normally due to limitations in the conductive network. As a result, the following cycle has an increased discharge capacity and a CE over 100 %. In both Figure 4.7c and 7d, method 3 batteries have the highest and most stable CE. A stable CE indicates minimized polysulfide shuttling, consistent conductive pathways, and stability under temperature fluctuations.[42] These advantages results from a robust SEI layer. We propose the robust SEI layer of Method 3 batteries traps polysulfides inside the SEI, causing a minimal amount of polysulfides to travel across the electrolyte and to the lithium counter electrode. This in turns reduces the damage polysulfides can cause to the lithium SEI while also reducing temperature impact on the electrolyte. This is in good agreement with Figure 4.7a and 7b, which show minimized capacity fluctuation in Method 3 batteries. Large difference exists between city and highway model CE becuase city model generates excess cycling stress compared to highway model. As shown in Figure 4.7a-c and 4.7d, higher testing stress causes increased capacity and CE degradation rate.

4.4 Conclusion

We have demonstrated three different conditioning methods for Li-S batteries to study their effects on formation of the SEI layer under varied cycling stresses. It was observed through the testing models, that plateau targeted conditioning (Method 3) creates a robust SEI layer on the sulfur and lithium electrode. We propose that this is attributed to the slower rate, targeting the second plateau, allocating more time for steady

formation of the SEI layer while reducing time spent in the first plateau associated with long chain polysulfides. The resulting SEI layer suppresses the diffusion of polysulfides out of the cathode onto the lithium electrode, improves ionic pathways, maintains mechanical integrity, increases capacity, and enhances cycling stability of the Li-S battery. Additionally, this technique bypasses the use of supplemental additives and their associated adverse effects. Future interests include physical and in-situ studies to further explore the benefits of conditioning. In conclusion, plateau targeted conditioning provides the field of energy storage a novel, facile approach to improve battery performance.

4.5 References

1. Wild, M., et al. "Lithium sulfur batteries, a mechanistic review." *Energy & Environmental Science* 8.12 (2015): 3477-3494.

2. Zhang, Sheng S. "Liquid electrolyte lithium/sulfur battery: fundamental chemistry, problems, and solutions." *Journal of Power Sources* 231 (2013): 153-162.

3. Islam, Md Mahbubul, et al. "ReaxFF molecular dynamics simulations on lithiated sulfur cathode materials." *Physical Chemistry Chemical Physics* 17.5 (2015): 3383-3393.

4. Cheon, Sang-Eun, et al. "Rechargeable lithium sulfur battery II. Rate capability and cycle characteristics." *Journal of The Electrochemical Society* 150.6 (2003): A800-A805.

5. Yamin, H., et al. "Lithium sulfur battery oxidation/reduction mechanisms of polysulfides in THF solutions." *Journal of the Electrochemical Society* 135.5 (1988): 1045-1048.

6. Mikhaylik, Yuriy V., and James R. Akridge. "Polysulfide shuttle study in the Li/S battery system." *Journal of the Electrochemical Society* 151.11 (2004): A1969-A1976.

7. Xiao, Lifen, et al. "A soft approach to encapsulate sulfur: polyaniline nanotubes for lithium-sulfur batteries with long cycle life." *Advanced materials* 24.9 (2012): 1176-1181.

8. Guo, Juchen, Yunhua Xu, and Chunsheng Wang. "Sulfur-impregnated disordered carbon nanotubes cathode for lithium–sulfur batteries." *Nano letters* 11.10 (2011): 4288-4294.

9. Chen, Shu-Ru, et al. "Ordered mesoporous carbon/sulfur nanocomposite of high performances as cathode for lithium–sulfur battery." *Electrochimica Acta* 56.26 (2011): 9549-9555.

10. Peng, Hong-Jie, et al. "Strongly Coupled Interfaces between a Heterogeneous Carbon Host and a Sulfur-Containing Guest for Highly Stable Lithium-Sulfur Batteries: Mechanistic Insight into Capacity Degradation." *Advanced Materials Interfaces* 1.7 (2014).

11. Papandrea, Benjamin, et al. "Three-dimensional graphene framework with ultra-high sulfur content for a robust lithium–sulfur battery." *Nano Research* 9.1 (2016): 240-248.

12. Wang, Hailiang, et al. "Graphene-wrapped sulfur particles as a rechargeable lithium–sulfur battery cathode material with high capacity and cycling stability." *Nano letters* 11.7 (2011): 2644-2647.

13. Bauer, I., et al. "Reduced polysulfide shuttle in lithium–sulfur batteries using Nafion-based separators." *Journal of Power Sources* 251 (2014): 417-422.

14. Peng, Hong-Jie, et al. "Enhanced electrochemical kinetics on conductive polar mediators for lithium–sulfur batteries." *Angewandte Chemie* 128.42 (2016): 13184-13189.

15. Millner, Alan. "Modeling lithium ion battery degradation in electric vehicles." *Innovative Technologies for an Efficient and Reliable Electricity Supply (CITRES), 2010 IEEE Conference on*. IEEE, 2010.

16. Kong, Weihe, et al. "Gas evolution behaviors for several cathode materials in lithium-ion batteries." *Journal of power sources* 142.1-2 (2005): 285-291.

17. Lin, Zhan, et al. "Phosphorous pentasulfide as a novel additive for high-performance lithium-sulfur batteries." *Advanced Functional Materials* 23.8 (2013): 1064-1069.

18. Wu, Feixiang, et al. "Lithium iodide as a promising electrolyte additive for lithium–sulfur batteries: mechanisms of performance enhancement." *Advanced Materials* 27.1 (2015): 101-108.

19. Scheers, Johan, Sébastien Fantini, and Patrik Johansson. "A review of electrolytes for lithium–sulphur batteries." *Journal of Power Sources* 255 (2014): 204-218.

20. Li, Weiyang, et al. "The synergetic effect of lithium polysulfide and lithium nitrate to prevent lithium dendrite growth." *Nature communications* 6 (2015): 7436.

21. Ji, Liwen, et al. "Porous carbon nanofiber–sulfur composite electrodes for lithium/sulfur cells." *Energy & Environmental Science* 4.12 (2011): 5053-5059.

22. Ding, Ning, et al. "Building better lithium-sulfur batteries: from LiNO 3 to solid oxide catalyst." *Scientific reports* 6 (2016): 33154.

23. Pang, Quan, Dipan Kundu, and Linda F. Nazar. "A graphene-like metallic cathode host for long-life and high-loading lithium–sulfur batteries." *Materials Horizons* 3.2 (2016): 130-136.

24. Liang, Xiao, Arnd Garsuch, and Linda F. Nazar. "Sulfur Cathodes Based on Conductive Mxene Nanosheets for High-Performance Lithium–Sulfur Batteries." *Angewandte Chemie International Edition* 54.13 (2015): 3907-3911.

25. Liang, Xiao, et al. "A highly efficient polysulfide mediator for lithium–sulfur batteries." *Nature communications* 6 (2015): 5682.

26. Pang, Quan, et al. "A Nitrogen and Sulfur Dual-Doped Carbon Derived from Polyrhodanine@ Cellulose for Advanced Lithium–Sulfur Batteries." *Advanced materials* 27.39 (2015): 6021-6028.

27. Xiang, Hongfa, et al. "Enhanced charging capability of lithium metal batteries based on lithium bis (trifluoromethanesulfonyl) imide-lithium bis (oxalato) borate dual-salt electrolytes." *Journal of Power Sources* 318 (2016): 170-177.

28. Tesla, Tesla.com. https://www.tesla.com/models, 2017 (accessed June 2017.June)

29. Chen, Jia-Jia, et al. "Conductive Lewis base matrix to recover the missing link of Li2S8 during the sulfur redox cycle in Li–S battery." *Chemistry of Materials* 27.6 (2015): 2048-2055.

30. Deng, Zhaofeng, et al. "Electrochemical impedance spectroscopy study of a lithium/sulfur battery: modeling and analysis of capacity fading." *Journal of The Electrochemical Society* 160.4 (2013): A553-A558.

31. Yan, Chong, et al. "Lithium metal protection through in-situ formed solid electrolyte interphase in lithium-sulfur batteries: The role of polysulfides on lithium anode." *Journal of Power Sources* 327 (2016): 212-220.

32. Delpuech, Nathalie, et al. "Mechanism of Silicon Electrode Aging upon Cycling in Full Lithium-Ion Batteries." *ChemSusChem* 9.8 (2016): 841-848.

33. Chang, Duck-Rye, et al. "Binary electrolyte based on tetra (ethylene glycol) dimethyl ether and 1, 3-dioxolane for lithium–sulfur battery." *Journal of Power Sources* 112.2 (2002): 452-460.

34. Markevich, E., et al. "On the Mechanism of Quasi-Solid-State Lithiation of Sulfur Encapsulated in Microporous Carbons: Is the Existence of Small Sulfur Molecules Necessary?." *Journal of The Electrochemical Society* 164.1 (2017): A6244-A6253.

35. Liu, Nian, et al. "A yolk-shell design for stabilized and scalable Li-ion battery alloy anodes." *Nano letters* 12.6 (2012): 3315-3321.

36. Skoog, Douglas A., F. James Holler, and Stanley R. Crouch. *Principles of instrumental analysis*. Cengage learning, 2017.

37. Su, Yu-Sheng, and Arumugam Manthiram. "A new approach to improve cycle performance of rechargeable lithium–sulfur batteries by inserting a free-standing MWCNT interlayer." *Chemical communications* 48.70 (2012): 8817-8819.

38. Ye, Rachel, et al. "Advanced Sulfur-Silicon Full Cell Architecture for Lithium Ion Batteries." *Scientific reports* 7.1 (2017): 17264.

39. Dees, Dennis W., et al. "Analysis of the Galvanostatic Intermittent Titration Technique (GITT) as applied to a lithium-ion porous electrode." *Journal of Power Sources* 189.1 (2009): 263-268.

40. Park, Min-Sik, et al. "Porous carbon spheres as a functional conducting framework for use in lithium–sulfur batteries." *RSC Advances* 3.29 (2013): 11774-11781.

41. Lee, Seung-Bok, and Su-Il Pyun. "The effect of electrolyte temperature on the passivity of solid electrolyte interphase formed on a graphite electrode." *Carbon* 40.13 (2002): 2333-2339.

42. Li, Nianwu, et al. "High-rate lithium–sulfur batteries promoted by reduced graphene oxide coating." *Chemical Communications* 48.34 (2012): 4106-4108.